Chapter 4

Coordinated HArd Sphere Model (CHASM): A simplified model for oxide liquids at mantle conditions

Abstract

We develop a new simplified model to understand and predict the behavior of oxide and silicate melts at extreme temperatures and pressures. The **C**oordinated **HA**rd **S**phere **M**odel (CHASM) is based on the extension of the hard sphere mixture model, accounting for the range of oxygen coordination states available to each cation in the liquid. By utilizing approximate analytic expressions for the hard sphere model, this method is capable of predicting complex liquid structure and thermodynamics while remaining computationally efficient, requiring only minutes of calculation time on standard desktop computers. We demonstrate how the parameters of the model can be obtained by training on equation of state data for a variety of crystal polymorphs, which discretely sample the range of available coordination states. This method is applied to the MgO system and then used to calculate the coordination evolution and equation of state of MgO liquid over a wide range of pressures and temperatures. The results produced by CHASM are finally evaluated by

comparison with predictions from published first-principles molecular dynamics calculations, indicating that CHASM is performing well and accurately capturing the dominant physics controlling the behavior of MgO liquid.

4.1 Introduction

Understanding the behavior of silicate liquids at mantle pressures is crucial to reconstructing the early evolution of Earth and other terrestrial planets. While molten silicates play a minor role in the deep mantle today, their material properties directly determined the Earth's evolutionary path as it cooled from a nearly whole-mantle magma ocean to its present-day solid state.

Recent first-principles theoretical calculations (*Stixrude et al.*, 2009) and experimental shock-wave investigations (*Mosenfelder et al.*, 2009) indicate that melting perovskite requires significantly less total energy than previously thought, supporting the idea of a deep potentially whole-mantle magma ocean early in Earth's history. The evolution of this magma ocean as it cools and crystallizes is dominated by the poorly understood behavior of silicates at extreme pressures and temperatures. Probing these conditions is difficult for both theory and experiment, and further challenges are posed by the large relevant compositional space, including at least MgO, $\mathrm{SiO_2}$, and spin-dependent FeO. The primary tool for theoretical work, first-principles molecular dynamics (FPMD), has been used to probe the behavior of a variety of silicate liquids including MgO (*Karki et al.*, 2006), $\mathrm{SiO_2}$ (*Karki et al.*, 2007), $\mathrm{Mg_2SiO_4}$ (*de Koker et al.*, 2008), $\mathrm{MgSiO_3}$ (*Stixrude and Karki*, 2005), and $\mathrm{Fe_2SiO_4}$ (*Ramo and Stixrude*, 2012). While extremely powerful, this approach has limitations including high computational cost, lower bounds on temperature due to relaxation constraints, as well as restrictions to length scales and time scales that are many orders of magnitude smaller than those relevant to the Earth or experimental methods.

As a compliment to accurate first-principles calculations, we have developed the **C**oordinated **HA**rd **S**phere **M**odel (**CHASM**), which represents oxide and silicate liquids by directly tracking the relative populations of differently coordinated cation species as a function of temperature and pressure. This model is based on extending the standard hard sphere mixture model (*Mansoori and Canfield*, 1969), which was recently applied to silicate liquids by *Jing and Karato* (2011). In order to reasonably represent compression-induced changes to internal energy, we implement a perturbation to the standard hard sphere model, in which the internal energy is represented by empirical pair potentials that are coordination dependent. Using the principle of free energy minimization, we determine the relative populations of the different coordination states. Since the hard sphere mixture model is a well-developed theory with trusted long-standing analytic approximations (*Mansoori and Canfield*, 1969), this minimization technique is computationally cheap, allowing rapid determination of the energies and coordination populations on a modern laptop computer, enabling in the near future complete mapping of the wide compositional spaces relevant to early Earth evolution. We also demonstrate how the well-known equations of state for a large set of solid structures can be used to determine appropriate values for the pair potentials, thereby raising making CHASM a fully predictive model for oxide liquids that does not require fitting liquid data.

4.2 Background

Understanding the behavior of liquids has been a challenge that has puzzled researchers for nearly a century. Since the need to understand and be able to predict liquid properties over a range of conditions is pervasive, progress has generally been distributed across a number of scientific disciplines, including thermodynamics and statistical mechanics, experimental geochemistry, and computational mineral physics. The primary research goals in each of these fields vary greatly, from gaining a mechanistic understanding of liquid properties, to providing an empirical description of compositional effects, to gaining a first-principles atomistic view of compression behavior for liquids with specific chemistries. Though each method is focused on a subset of the overall problem, together they contribute useful and complimentary insights to our understanding of liquids under a range of conditions. To provide context for the new model development described here, we give a short review of the existing approaches to modeling and measuring liquid properties from these different fields.

4.2.1 Ideal Mixing Models for Experimental Data

We start with the simplest possible model for liquid thermodynamics, which considers a set of endmember compositions that mix ideally. While this method is computationally simple, it relies on accurate and difficult to obtain experimental measurements of the properties of a range of liquids of different compositions. Such experiments include ambient pressure sound speed measurements, like those reported in *Ai and Lange* (2008), and measurements of density and internal energy in ultra high-velocity shock-wave experiments, like those of

Asimow and Ahrens (2010) and *Thomas et al.* (2012). Given a measurement of the volumes and energies of liquids for a range of compositions at a particular P-T condition, the ideal mixture model supposes that the volumes, entropies, and energies are additive and depend linearly on the fraction of each end-member composition (*Bottinga and Weill*, 1970). This assumption supposes that the excess energy and excess volume of mixing are both negligible and that the entropy of mixing is well described by simple ideal mixing of end-members. While this method employs a strong assumption of ideality, it is shown to perform fairly well under many conditions. One major difficulty with this method is that it requires extensive data sets for liquids spanning large ranges in composition in order to uniquely constrain the behavior of the endmembers. Additionally, it is fairly limited in its ability to extrapolate beyond the experimental pressure and temperature conditions, providing instead a sensible method for interpolation between data points. Even so, the ideal mixing model has found great success at describing the thermodynamics of complex many-component oxide and silicate liquids, as presented in *Ai and Lange* (2008), for instance.

Despite extensive success, there are notable shortcomings to the straightforward application of this approach, as explored by (*Guo et al.*, 2013), in which they show evidence for large changes in the partial molar volume of the iron oxide component as a function of overall composition. In particular, this change is interpreted as a strong composition dependence to the oxygen coordination number of iron, which thereby exerts large controls over the volume of the solution since 6-coordinated iron is significantly more compact than 4-coordinated iron. It is possible that the ideal mixing approach can remain useful in such cases by including separate endmembers that explore the different dominant coordination states for each cation, though the simplicity and predictive power of the method could suffer as a result. Preliminary results from shock-wave experiments on liquids in the $\mathrm{CaO{-}MgO{-}Al_2O_3{-}SiO_2{-}FeO}$ system show similar failures of the ideal mixture method (*Thomas et al., submitted* 2013), though it is not yet clear whether the practical approach of adding more end-members that sample the range of dominant coordination states is sufficient to address shortcomings of the approximation.

4.2.2 Atomic Simulation Using Molecular Dynamics

An entirely different and theoretical approach is to perform molecular dynamics simulations to directly track the motions of the atoms that make up the liquid. In this method, the trajectories of a finite number of atoms are evolved within a simulation cell. Periodic boundary conditions are imposed on the simulation, mimicking an effectively infinite tiled domain composed of side-by-side repeated images of the simulated region. Using basic Newtonian mechanics, the positions and velocities of each atom are updated in response to the imposed forces, which result from complex electronic interactions. The method of determining the forces at each time step separates this approach into two possible forms: Empirical Potential Molecular Dynamics (EPMD) versus First-Principles Molecular Dynamics (FPMD).

In the empirical approach, the interactions amongst the atoms are parameterized in terms of analytic potentials, typically using standard forms that capture the general features of atomic interactions. In the simplest and most common form, only pairwise additive interactions are considered, yielding pair potentials which are typically composed of a sum of repulsive and attractive terms. Since these equations are simple analytic expressions, the evaluation of energies and forces at each time step is comparatively rapid, and therefore EPMD is typically capable of representing between 10^4 and 10^5 atoms per simulation cell over relatively moderately long simulation times of order few nanoseconds. The major challenge with EPMD relates to whether that the parameter values for the empirical potentials are applicable outside the conditions under which they were trained and thus the quality of the simulation results can vary widely, depending on the details of the system. Improvements to accuracy can often be made by including many-body terms in the interaction energies, which can be important for determining bonding and coordination effects in many liquids *Daw et al.* (1993). Despite the challenges involved in training atomic potentials that are capable of remaining accurate over large compression ranges, there have been a few studies that apply this method to high-pressure systems, though agreement with experiment tends to break down at higher pressures (e.g., *Spera et al.*, 2009).

First-Principles Molecular Dynamics (FPMD) avoids many of these issues surrounding accuracy of the applied forces by determining them directly using first-principles quantum mechanics calculations. This strategy has gained much popularity over the last decade, as computational resources have become more powerful and affordable. In this approach, the forces imposed by the electron cloud distributions at each time step are determined self-consistently using Density Functional Theory, a practical quantum mechanical method that can provide approximate solutions to Schrödinger's equation. While accuracy is obviously less of an issue, this approach imposes a significantly higher computational burden, requiring long calculations times on parallel processor machines. Capable of handling only a handful of atoms (of order 10^2 to 10^3), it is limited to small simulation cells with length scales of roughly 10 angstroms, short evolution times of the order of picoseconds, and high temperatures above 3000K, in order to remain computationally feasible. This means that liquid behavior can only be modeled for temperatures well above the liquidus, thereby avoiding impossibly long equilibration times. In such analyses, it is implicitly presumed that picosecond evolution times for at most 1000 atoms are sufficient for accurate thermodynamic averaging. While this is likely adequate for equation of state properties of most systems, any physical effects that rely on length scales approaching the size of the simulation cell will not be captured by this approach, making the determination of dynamic material properties like diffusivity and viscosity potentially much more uncertain.

Despite these limitations, this method has been found to be extraordinarily useful, and there have been numerous recent studies on high-pressure Mg-silicates using FPMD, covering a finite set of compositions across the $\mathrm{MgO-SiO_2}$ join (see, for instance, *de Koker et al.*, 2013). By focusing on a particular fixed composition and calculating the time-averaged free energies for a small set of volumes and temperatures, investigators are able to fit parametric equation of state forms to describe that liquid over a continuous pressure-temperature region. Due to computational limitations, the FPMD approach is therefore focused on simulating the detailed high-temperature behavior of a small set of particularly interesting liquid compositions.

4.2.3 Basic Hard Sphere Model

The search for a simple mechanistic model to describe liquids traces all the way back to the birth of our understanding of the molecular nature of matter, to the work of Johannes Diderik van der Waals in 1873. In his investigations of the behavior of fluids at very high temperatures, he sought an explanation for the disappearance of the vapor to liquid transition upon compression (for temperatures above the critical point). This led him to develop an improved equation of state, the familiar van der Waals equation:

$$P = \frac{RT}{V-b} - \frac{a}{V^2} \tag{4.1}$$

In proposing this expression, van der Waals hypothesized that a fluid is composed of equivalent discrete particles of matter (molecules). Due to their finite size and rigidity, the molecules that make up the liquid are forced into non-overlapping configurations, which therefore reduces the free volume, which describes the fraction of the volume available for the molecules to occupy. In the first term of his equation, van der Waals replaced the volume in the ideal gas equation with an effective free volume, which is just the total volume V less the excluded volume b due to the molecules, $V_{\text{free}} = V - b$. The second term represents weak attractive forces—now referred to as van der Waals forces—that help bind the fluid together and can be represented to leading order as proportional to $1/V^2$. With this equation, van der Waals was able to represent the critical behavior of fluids, but more importantly, he laid the groundwork for understanding liquid thermodynamics in terms of effects resulting from the finite size of fluid particles.

Nearly a century later, the idea of representing a fluid as a collection of hard spheres experienced a sudden renaissance with the advent of large computing resources. As hinted by the early success of the van der Waals equation, the behavior of liquids is dominated by strong short-range repulsive forces that prevent liquid particles from occupying the same space. Therefore, the behavior of liquids can be represented using a simple hard-wall potential function:

$$\Phi_{ij}\left(r\right) = \begin{cases} \infty \quad ; \quad r < R_i + R_j \\ 0 \quad ; \quad r \geq R_i + R_j \end{cases} \tag{4.2}$$

where the internal energy Φ_{ij} of particles i and j is zero for all non-overlapping configurations. Particle overlap is expressly forbidden by a jump to infinite energy when their separation distance is less than the sum of their radii $r < R_i + R_j$. This almost trivial equation is the basis of the hard sphere model, which has been the source of a wealth of information about the general properties of liquids. The initial investigations of hard sphere fluids represented some of the first computer simulations ever performed. Later efforts by many investigators provided analytic expressions that approximate the results of these computational simulations to high degrees of accuracy. It is these analytic expressions which make the hard sphere model so attractive, since they enable rapid calculation of liquid properties many orders of magnitude faster than molecular dynamics simulations and on standard personal computers rather than large super-clusters.

We can intuitively understand some of the basic properties of the hard sphere model and liquids in general by examining snapshots of hard sphere fluids at different packing fractions. At ambient conditions, the internal energy of a liquid plays only a very minor role in determining liquid thermodynamics—instead, the dominant term in the free energy of the system comes from the configurational entropy resulting from the freedom of liquids to adopt nearly any structure that avoids particle overlap. In particular, quantities like the expected particle separation distance and pressure for a given volume are primarily dependent on the number of available microstates or configurations that exist for a particular set of macroscopic variables (e.g., volume and temperature). This structural freedom is cast in terms of the free volume available for each particle to move through. At the relatively low densities near vapor equilibrium considered by van der Waals, the free volume is shared by all liquid particles and is thus simply the total volume less the excluded volume, as reflected in the van der Waals' equation. It is important to note that the excluded volume is larger than the volume occupied by liquid particles. For low density configurations of hard spheres, the closest two particle centers can get to one another is the sum of their radii. This results in an excluded region for a pair of particles that has a radius of twice the sphere radius, and thus eight times the volume. On a per particle basis, the excluded volume is therefore four times the particle volume for disperse particles, as was noted by van der Waals. This approximation breaks down, however, for dense packings, where each liquid particle can have multiple nearby neighbors. In such tightly packed configurations, the excluded volume regions of neighboring particles overlap one another, resulting in a total excluded volume that is only a fraction of van der Waals' upper limit.

To visualize the effect of packing density on the excluded volume, Figure 4.1 shows a snapshot of a 2D hard sphere fluid at a range of liquid densities. The relative liquid density

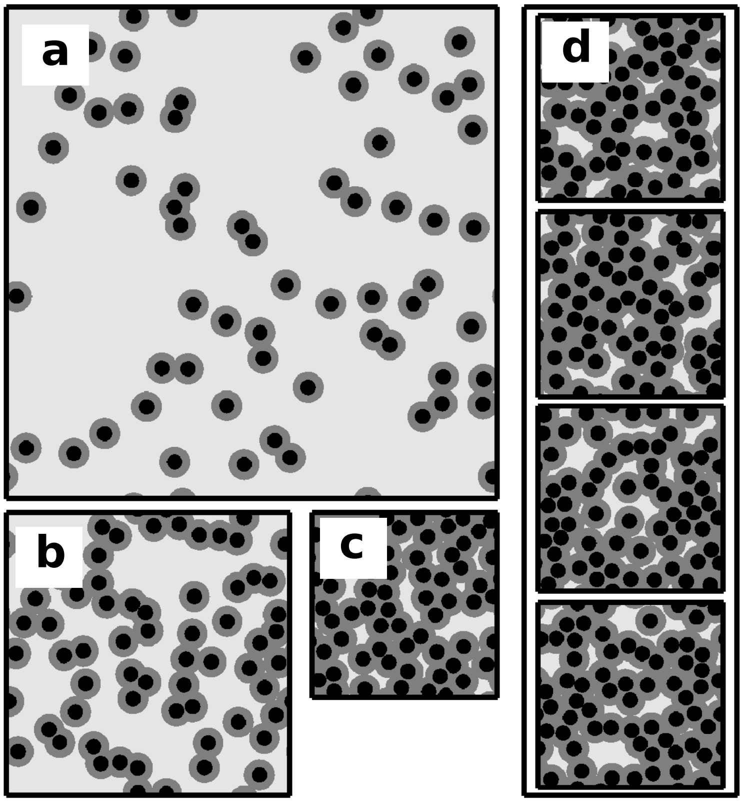

Figure 4.1: Snapshots of the simple hard sphere model for a range of packing fractions. Each hard sphere particle is show in black and the gray halo around it represents the excluded volume region that other particle centers are prevented from occupying. Panels a–c span the range of packing fractions from nearly ideal non-interacting fluids to extremely dense liquids. Panel d shows a variety particle configurations at fixed density.

is expressed in terms of the packing fraction

$$\eta \equiv \frac{\langle V_{\mathrm{HS}} \rangle}{V} = \frac{1}{V} \frac{4\pi}{3N} \sum_{i}^{N} R_i^3 \tag{4.3}$$

which is just the average hard sphere volume V_{HS} scaled by the volume of the liquid per particle, V. In the single component hard sphere fluid, the expression simplifies since all particles have the same fixed size. [1] Each sphere is shown in black with a gray halo around it representing the potential excluded volume region. In the disperse (gas-phase) limit, shown in panel a of Figure 4.1, particles generally lie far from one another interacting through collisions only rarely. In this case, the finite particle volume is negligible, and therefore particles can be treated as point-like, resulting in ideal gas behavior. For moderate packing fractions (low density liquid phase), particles regularly interact with one another revealing the importance of the excluded volume. As shown in Figure 4.1 panel b, particles at these moderate densities tend to have only one or two immediate neighbors, and therefore the excluded volume is approximately additive. For high packing fractions (high-density liquid phase), particles are forced to significantly crowd together, causing their excluded volume regions to strongly overlap, as seen in panel c of Figure 4.1.

A crucial attribute of liquids that relates directly to the excluded volume effect is the dependence of excluded volume on configuration. To demonstrate this, a number of random snapshots at constant packing fraction are shown in panel d. From these images, it can be seen that the evolving random liquid structure leads to fluctuations in the total ex-

---

[1] It should also be noted that all of the figures depicting snapshots of hard sphere configurations are shown for explanatory purposes, created from calculations of 2D hard sphere liquids. All of the equation of state calculations are carried out properly in three dimensions using the analytic approximate methods reviewed in the Appendix.

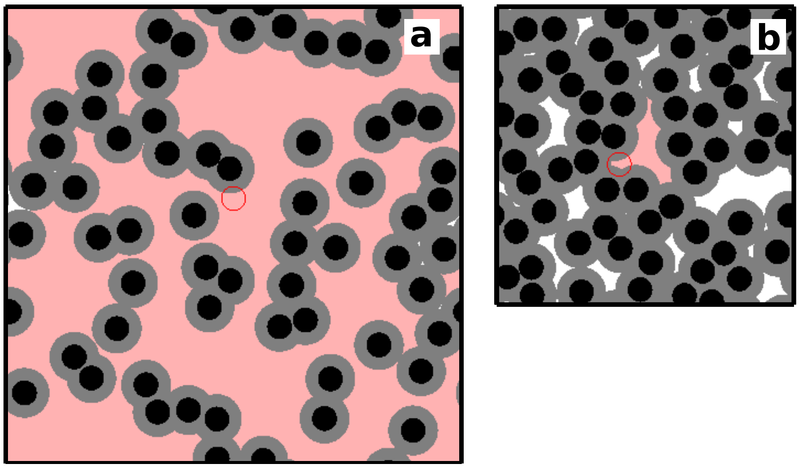

Figure 4.2: Snapshots of a hard sphere fluid at moderate (a) and high (b) packing fractions. These configurations are identical to panels (b) and (c) of Figure 4.1, but a single particle, outlined in red, has been removed. The light red shaded region shows the free volume available to the reference particle. At low packing fractions (a), particles all share the same free volume, whereas at high packing fractions (b), each particle is trapped by its neighbors.

cluded volume as well as the locally available free volume, shown in white. As the particles bounce around in the fluid, the degree of overlap between their excluded volume regions evolves as a function of configuration, resulting in complex sub-additive behavior for the total excluded volume of the liquid. Another consequence of tightly packed configurations is that particles no longer share the same free volume. In Figure 4.2, we repeat two of the same configurations from the previous figure, but in this case, one of the particles has been removed to display the local instantaneous free volume available for it to explore. The location of the removed particle is shown with a red outline near the center of the simulation cell, and its local free volume region is shaded in light red. In the low density case, the particle can access nearly the entire free volume of the liquid. In the high density case, however, the particle is confined within an instantaneous “cage” formed by its neighbors. This leads to equations of state and average liquid structures that have complex dependencies on the packing fraction. It is quite remarkable that such complex behaviors such as the sub-additivity of excluded volumes and the evolution of particle-specific free volumes can be well represented by the simple hard sphere fluid.

4.2.4 Previous Application of Hard Spheres to Silicate Liquids

The hard sphere model has been investigated through both computer simulation and analytic theoretical development over the last half-century. This has resulted in a rich and mature body of literature that is readily available for applications to any particular problem of interest. For the sake of brevity and readability, we will wait to present these classic results for hard spheres until it becomes relevant to our modeling efforts. We do want to draw attention, however, to the wealth of analytic approximations that are now available to describe many different aspects of the hard sphere model. These include fundamental thermodynamic relations like the equation of state, which relates the volume and the temperature to the pressure. The time-averaged structure of hard sphere fluids is also known analytically. Unlike crystalline solids that have fixed and periodic structures, liquids present a time evolving continuum of relative atomic positions. In order to handle this ambiguity, the average liquid structure is usually described in terms of the radial distribution function (RDF), which expresses the average local density of particles at a given separation distance relative to the density of the liquid as a whole. Most important for real-world applications is the fact that these properties are also known for random mixtures of hard spheres of varying sizes.

Given that most of the primary thermodynamic results for hard spheres have been in place for almost 40 years, it is rather surprising that hard sphere theory is rather new to the study of silicate melts. The first notable application of hard spheres to silicate liquids was presented by *Guillot and Sarda* (2006), in which they modeled the compression of particular fixed composition silicate liquids in order to investigate the solubility behavior of noble gases. In this first application of hard sphere theory to geologically relevant materials, *Guillot and Sarda* (2006) obtained the compression behavior for MORB, silica, and olivine composition liquids up to 10 GPa. This was accomplished by determining a single effective hard sphere size for each liquid that best matched a measurement of the 1 bar density at a reference temperature. It is important to note that this method yields only a very approximate description since it relies on representing each liquid as a collection of identical hard spheres, where it is unclear which structural aspects of a multicomponent liquid this physically represents. Even more important is the fact that this method is limited only to describing liquids at particular fixed compositions for which data already exists, and is therefore incapable of producing a predictive theory for liquids with unmeasured compositions. Nevertheless, this approach was reasonably successful at fitting low degree compression data with only a single free parameter.

More recently, *Jing and Karato* (2011) made considerable progress in the hard sphere description of silicate melts by fitting a set of hard sphere diameters to a collection of liquid density measurements in the $\mathrm{CaO{-}MgO{-}Al_2O_3{-}SiO_2{-}FeO}$ system. To accomplish this, they utilized an analytic approximate result for describing mixtures of hard spheres of different sizes (*Lebowitz*, 1964). (This classic work derived a generalized expression for the Percus-Yevick equation, which describes the radial distribution function for hard spheres, to allow for a random mixture of differently sized spheres.) Unlike the previous geological application, it is somewhat easier to draw a tie between the hard spheres of *Jing and Karato* (2011) and the physical aspect of the liquid they represent. They obtained a set of best-fit sphere sizes, where each sphere stands for a particular oxide component, like $\mathrm{SiO_2}$ or MgO. Since the spheres are meant to represent the relatively incompressible local units of the liquid, and they are specific to each oxide component, we can think of them as the region surrounding a cation and including a fraction of the shared oxygens that are directly bonded to that cation.

In order to obtain the oxide sphere sizes, *Jing and Karato* (2011) fit a large data catalog of liquid densities and bulk moduli (from sound speed measurements) for a range of temperatures and compositions at ambient pressure. Initially, they found the fixed hard sphere diameters that best matched the liquid data in the least-squares sense. Later in the paper, they also added in a physically motivated correction for temperature, which has often been applied in the hard sphere literature with moderate success, and an entirely empirical correction for pressure, to attempt to better match high-pressure shock-wave measurements. By including the temperature correction, they were able to demonstrate quite compellingly that they were able to reproduce the generally observed trends in density and compressibility for a large chemical system at ambient pressures. Using the empirical correction to allow the spheres to be slightly deformable with increasing pressure, they were also able to match low-pressure data up to 25 GPa from sink/float experiments. By adding a further empirical term to the pressure-dependent deformability of the spheres, they could better describe a small set of shock-wave measurements up to 135 GPa, but as all of these correction factors are no physically motivated, they can only provide modest improvements without adding significant insight. As the authors remark themselves, it would be better to be able to directly represent the compression-induced structural changes that are physically occurring within the liquid in order to have a theory with greater predictive and explanatory power.

4.2.5 Local Liquid Structure

As discussed in the previous section, efforts to adapt hard sphere theory to silicate melts up till now have focused on empirical determination of hard sphere parameters. Using this method, *Guillot and Sarda* (2006) and *Jing and Karato* (2011) were able to lean on the formalism of hard spheres to act as a physically motivated "averaging kernel", allowing them to effectively interpolate within the data set upon which the hard sphere sizes were trained. Extrapolation outside the training set, however, was fairly limited, as the hard spheres were not strongly connected with physically meaningful aspects of the liquid structure. It is for this reason that neither model was capable of accurately representing large compression ranges, with pressures over 30 GPa being generally inaccessible. Furthermore, any compositionally induced structure changes in liquids would also fall outside the capabilities of this approach. In the process of developing a more physically rooted application of the hard sphere model, we therefore have strong motivation to consider the structural attributes of dense silicate melts with a focus on how they are affected by changes in pressure and composition.

While studying atomic structure in melts is more difficult than in crystalline solids, there exist a number of methods that can be brought to bear in this effort. We start by describing the method that is the most directly sensitive to atomic structure, and is thus the primary tool for probing crystalline solids: x-ray or neutron diffraction. Each atom in the material acts as a scattering center for incoming high energy particles (typically photons or neutrons). Due to its wave-like nature, the phase of the incoming radiation is retained upon scattering, allowing the radiation from the collection of atoms in the material to add constructively or destructively. The general condition for constructive interference is that the path length traveled by a set of scattered rays is equal to an integer number of wavelengths. When considering a periodic crystalline structure, this is typically stated in terms of the spacing between adjacent crystal planes, d, in terms of Bragg's Law:

$$n\lambda = 2d\sin\theta \tag{4.4}$$

where λ is the wavelength of radiation used to probe the structure, n is the order of the reflection (typically $n = 1$ for most diffraction data since higher order reflections have negligible intensity), and 2θ is the scattering angle, defined as the angle between incoming and diffracted rays. From this equation, it is clear that radiation is scattered at high intensity into only a finite set of preferred directions which are characteristic of the crystal structure.

Liquids, on the other hand, are significantly more complex than crystalline solids since they lack periodicity. They, therefore, do not have large sets of atoms at precise locations from which coherent scattering can lead to sharp and intense diffraction peaks. Rather, they contain a collection of disordered atoms which lie at random absolute locations in space, reflecting a lack of long-range order. Nevertheless, the atoms occupy characteristic locations relative to one another, reflecting their considerable short-range order. As briefly mentioned above, the probabilistic nature of the structure of liquids is best-described in terms of the Radial Distribution Function (RDF), $g(r)$, which is proportional to the probability, $P(r)dr$, of finding two atoms a given distance apart:

$$g(r) \equiv \frac{\rho(r)}{\langle\rho\rangle} \quad \text{and} \quad P(r)dr = 4\pi r^2 \langle\rho\rangle g(r) dr \tag{4.5}$$

The RDF therefore gives the typical particle density a distance r away from a reference particle, normalized by the average density $\langle\rho\rangle$. The RDF is easily calculated from atomic simulations by counting the number of particles inside a set of thin spherical shells of varying sizes and averaging over the all particles and time-steps. Figure 4.3 shows a typical RDF for a simple monatomic liquid depicting the two primary features of average liquid structure: a sharp inner edge to the particle density and decaying density oscillations with increasing distance. The inner edge is roughly equal to the sum of particle radii and simply results from finite particle size and the corresponding tendency of particles to avoid overlapping one another. The decaying density oscillations about the average value reflect the limited short-range order in the liquid, where each subsequent maximum corresponds to the next-nearest-neighbor shell of particles, and at sufficient distance, all ordering tendency is lost yielding the average density value.

While the radial distribution function is not a direct observable for real-world liquids like it is for atomic simulations, it is nevertheless closely related to the data produced by x-ray or neutron diffraction. By replacing periodic lattices with a tendency toward local ordering, diffraction experiments for liquids result in a characteristic broad, low intensity pattern referred to as "diffuse scattering", which displays azimuthal symmetry and slow os-

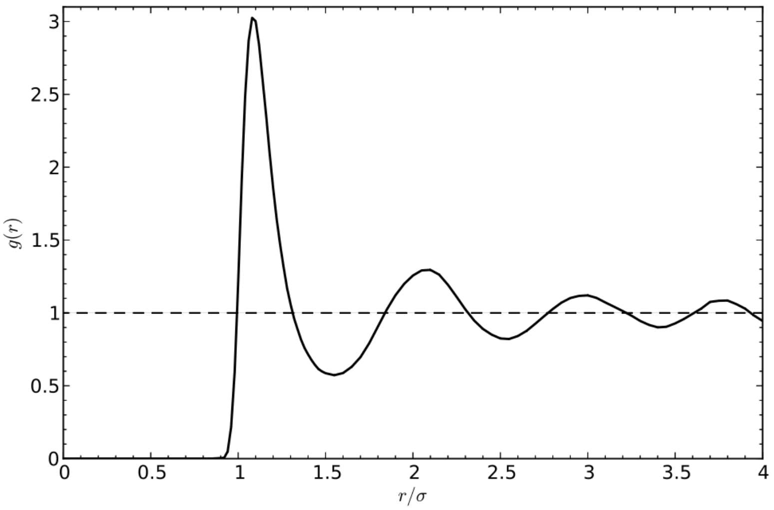

Figure 4.3: Depiction of the radial distribution function (RDF) of a simple model liquid (in this case the Lennard-Jones fluid). The primary features of the RDF are its primary peak, indicating the average nearest-neighbor particle distance, and its decaying oscillations, reflecting successive shells of neighboring atoms which become less distinct with distance as long-range disorder comes to dominate. [image credit: wikipedia.org]

cillations in intensities as a function of the scattering angle. The integrated 1D diffraction pattern can be straightforwardly transformed into the structure factor, which is a normalization of the scattered intensity giving the absolute scattering per atom as a function of the scattering vector $\vec{q} = \vec{k}_{scat} - \vec{k}_{inc}$ (the difference between the scattered and incident wavevectors). The structure factor for a liquid bears a strong resemblance to its radial distribution function, reflecting the fact that they are Fourier transforms of one another. The basic structural depiction of liquids can therefore be obtained with minimal processing of diffraction data.

Challenges arise from the fact that, unlike its crystalline counterpart, the diffuse scattering pattern is inherently broad and low intensity, making it easily confused with the similarly broad yet unconstrained background pattern. It is therefore only with great difficulty, taking care to minimize background signal using large samples and careful experimental designs, that reliable liquid structure factors are obtained. It is with even greater difficulty that structure factors can be measured for high-temperature, high-pressure liquids like silicate melts (*Funamori et al.*, 2004). It is for this very reason that much of our knowledge of liquid structure relies on insights gained from quenched glasses.

Glasses are strongly preferred to melts for most analytic techniques since they can be measured at ambient conditions on large stable samples. Glasses form as a result of rapid cooling of the liquid, where the cooling timescale is shorter than the kinetic relaxation timescale, forcing the liquid to fall out of equilibrium and thereby freezing its structure. By imposing a range of cooling rates, experimentalists can obtain a set of snapshots of the liquid structure at different temperatures, where the effective temperature at which the liquid structure is frozen into a glass is called the “fictive temperature”. These different cooling rates are achieved using a variety of cooling methods, which include (in order of increasing cooling rate): slow controlled cooling by reducing furnace power over time, air cooling where the melt is removed from the furnace, water cooling where it is submersed in a water-bath, and splat quenching where melt is squirted at high speed onto freezing cold metal. By varying the cooling rate over ten orders of magnitude through such techniques, the fictive temperature can be adjusted by typically of order a few hundred degrees for silicate glasses. Some of these techniques can also be adapted for use in a high-pressure, high-temperature apparatus like a multi-anvil furnace to generate glasses from high-pressure silicate melts. These glasses are then available for conventional measurements, like the diffraction determined Radial Distribution Functions described above.

There is also a broad set of spectroscopic techniques that can been used to probe the local environment of particular atoms in liquids and quenched glasses. These methods rely on a variety of complex interactions between photons of different wavelengths and the nuclei or electron distributions inside the material. Without going into the details, we briefly mention some of the available techniques and the general insights they provide about high-pressure silicate melts. Nuclear magnetic resonance spectroscopy is one of the most successful techniques for probing the local environment around certain target atoms within a material. This term is actually used to describe a wide set of methods that exploit the properties of certain nuclei and their tendency to couple with and react to externally imposed strong magnetic fields. For particular set of atoms, it is possible to observe emitted photons that are characteristic of different properties of the local environment about the nucleus, using a variety of specially designed magnetic fields that may vary in space, time and orientation. For Earth scientists, measurements of silicate materials using ^{17}O-, ^{27}Al-, and ^{25}Mg-NMR have proved particularly useful in studying the evolution of coordination state (number of bonded nearest neighbors) as a function of both pressure and composition. There have been numerous studies over the last two decades that have examined the evolution of oxygen coordination of the Al cation increasing smoothly with increasing pressure (see, e.g., *Lee*, 2011). Typically these studies rely on measurements of quenched glasses rather than in situ high-temperature melts, but it is quite clear that the smooth shift in coordination populations to higher values with increasing pressure is the dominant compression mechanism of most oxide liquids over mantle pressure ranges. In particular, ^{27}Al-NMR studies of Al-silicate glasses are particularly useful since aluminum often substitutes in for silicon within the polymerized network of the silicate structure. By

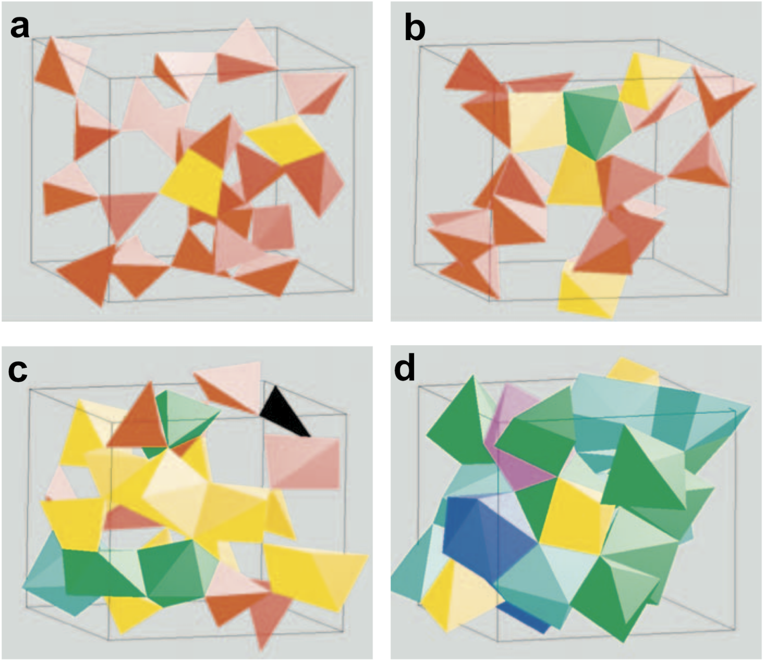

Figure 4.4: Evolution of $\mathrm{Si-O}$ coordination polyhedra with increasing compression. Snapshots are shown for a range of volumes, relative to the initial reference volume, (1.0, 0.8, 0.6, 0.4) and a range of temperatures (3000K, 4000K, 5000K, 6000K). Dominantly 4-coordinated Si gives way gradually to 6-coordinated Si with compression. [image credit: *Karki et al.* (2007)]

examining the shift from dominantly 4-coordinated aluminum at ambient conditions up to 5- and 6-coordinated Al, we can gain insights about the general shifts occurring in the liquid's silica framework.

The last primary way in which local liquid structure is probed is through molecular dynamics simulations like those discussed in Section 4.2.2. By turning to FPMD techniques, researchers can obtain reasonable predictions of both liquid structure and thermodynamics at extreme temperatures (above ~ 3000 K) and high pressures that are unattainable in most experimental setups. Such high temperatures pose great difficulties for in situ measurements and quenched glasses are restricted to fictive temperatures with a theoretical maximum at the liquidus ranging down to a few hundred degrees below. Additionally, rapid quenching is made more difficult inside high-pressure apparatuses like multi-anvil presses or diamond anvil cells. Atomic simulation, with its direct knowledge of the exact position of each atom in the fluid, therefore, has a large role to play in the evaluation of liquid structure. The general results from FPMD studies of terrestrial liquids at mantle conditions support the same general conclusions of the diffraction experiments and spectroscopy studies. For visualization purposes, we reproduce a figure from *Karki et al.* (2007) shown in Figure 4.4, which shows the evolution of the different $\mathrm{Si-O}$ coordination polyhedra with increasing compression. As can be seen in the first panel, at a volume V_X corresponding to ambient pressure at 3000K, the Si cations lie predominantly in a tetrahedral 4-coordinated state, and as pressure is increased they gradually shift toward higher coordination numbers, occupying primarily octahedral 6-coordination state at 6000K and $V = 0.4 V_X$. It should also be noted that the variety of simultaneously occupied coordination states increases with increasing temperature, as expected from simple Boltzmann-like statistical considerations. In fact, not only is coordination evolution the primary compression mechanism for pure silica, it is found to actually fight against bond length changes, where the nearest-neighbor silicon-oxygen bond length is seen paradoxically to initially *increase* on compression, indicating just how strong the energetic benefit to increasing coordination actually is. Similar coordination behavior has been seen across many different compositions relevant to rock-forming liquids including MgO (*Karki et al.*, 2006), all along the MgO—$\mathrm{SiO_2}$ binary (*de Koker et al.*, 2013), and $\mathrm{Fe_2SiO_4}$ (*Ramo and Stixrude*, 2012).

4.3 Coordinated HArd Sphere Model (CHASM)

Given the combined evidence from diffraction studies, NMR spectroscopy, and FPMD simulations, it appears that oxygen coordination evolution is a common compression mechanism across all high-pressure oxide and silicate melts. Despite this fact, there does not currently exist a simplified theory for oxide melts which accounts for the coordination effects that dominate compression throughout the Earth's mantle. We therefore develop a simplified model to represent high-pressure oxide liquids that explicitly accounts for the range of available coordination states for each cation, and thereby predicts the evolution of coordination with changing pressure, temperature, and composition. The **C**oordinated **HA**rd **S**phere **M**odel (CHASM) provides a general framework for representing the compression behavior of silicate and oxide liquids in terms of evolving the relative populations of different oxygen coordination states for each cation in the liquid, using a perturbation to the hard sphere mixture model. Furthermore, by exploiting the analytic expressions for mixtures of hard spheres from the physics and statistical mechanics literature, we construct a model that captures the basic physical mechanisms while remaining computationally efficient, being easily run on a standard personal computer in minutes, rather than taking months on multi-node supercomputers. Following the classic approach of training empirical potentials, this is a model that relies on parameters that are determined from the comparatively well-understood behavior of solid polymorphs, and can thus be fully predictive for silicate liquids.

4.3.1 A Qualitative Picture of Liquid Compression

To introduce the basic concepts important to constructing such a model, we first examine the essential differences between compression in solids and liquids and how this relates to their respective equations of state. In Figure 4.5, we show a two-dimensional cartoon representation of the compression of materials along a continuum from solid-like to liquid-like behavior. (It should be noted that while this diagram is only meant to illustrate the important concepts, it has been constructed properly using a Monte Carlo hard sphere model to represent liquid particles of different sizes.) Each panel of the figure show two snapshots of the particle structure in the material at particle densities relevant to low- and high-pressure states in light and dark gray, respectively.

Up to this point, we have used a variety of terms, including atom, molecule, or "particle", to refer to the matter making up the liquid. Generally speaking, a liquid particle should be thought of as the smallest structural unit that can be used to describe the liquid. Oftentimes, these are simply atoms or molecules. In the case of ionic liquids, like the silicates and oxides that are the focus of this study, the particles should be thought of as cation-anion groupings. In order to minimize the Coulombic energy, the large oxygen anions remain grouped around each central cation even in the liquid state, where the number of nearest-neighbor oxygens about each cation is expressed through the coordination number of that cation. As time progresses, the cations and oxygens both move through space, causing both the coordination number and the identity of the coordinated oxygens to evolve with time. Nevertheless, the energy penalties for segregating the oxygens and cations are so high that each cation is always surrounded by an ever-changing local shell of oxygens

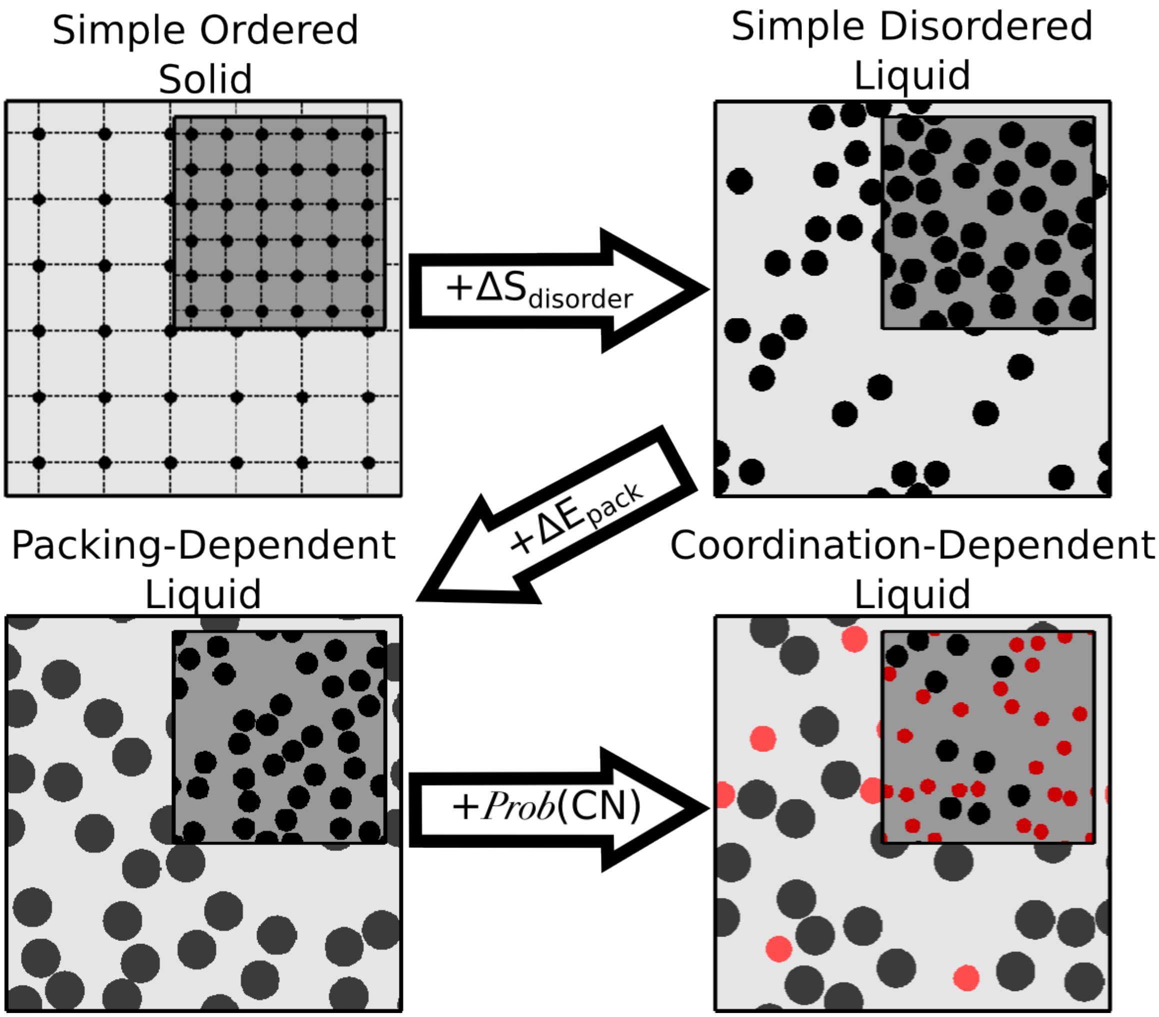

Figure 4.5: Compression mechanism cartoon for oxide liquids showing the different conceptual steps involved in getting from solid-like compression to liquid-like compression. We start with simple ordered solid compression, where all volume changes are taken up by changing bond lengths. The addition of considerable entropy upon melting leads to a simple disordered liquid that can be described with the hard sphere model. Including dependence of the internal energy on packing fraction results in a perturbed hard sphere model, where the sphere sizes adjust with compression. Finally, allowing for varying coordination states with populations that depend on packing fraction yields a reasonable picture of a coordination depend liquid. In the final panel, high and low coordination are shown in red and black, respectively, and the liquid adjust the coordination populations toward higher coordination states with increased compression.

and can be usefully described as evolving through a series of coordination states. (In reality, the oxygens also undergo some coordination evolution, increasingly being shared by 3 instead of only 2 cations, but this has a less major impact on the overall liquid thermodynamics.) In this way we can adapt the hard sphere model to ionic liquids by thinking of the spheres as representative of coordinated ionic complexes, where each is centered on a single cation. The interactions of each sphere with its neighbors is therefore governed primarily by its coordination state, which affects both the size of the complex and the way in which it is connected to its neighbors through the background field of oxygens that are implicitly present and surrounding each cation.

Keeping this understanding of liquid particles in mind, we can look to Figure 4.5 to gain an intuitive grasp of the mechanisms that operate in liquids to accommodate compression and how they differ from compression in solids. In the upper left of the figure, we start with the orderly compression of solids, which is dominated by changes in bond length. With atoms fixed in their relative positions within the unit cell, compression in solids is marked by only small changes in disorder associated with the decreasing volume available for thermal atomic vibrations. Upon melting, materials gain a significant bump in entropy, associated with the loss of long-range order. As discussed above, liquids still maintain short-range order, which can be approximately represented using the basic hard sphere model. This simple disordered liquid is depicted in the second panel of Figure 4.5, where the changes in the liquid structure are controlled by the packing fraction. It is important to note that in this case, the hard sphere radius is assumed to be fixed and independent of both temperature and compression. A simple hard sphere model such as this is the type utilized by *Jing and Karato* (2011) to describe low-pressure silicate liquids.

A further refinement to the physical picture can be made by including the feedback effect of compression on the excluded volume. In the third panel, we show how a more realistic liquid picture allows the sizes of the hard spheres particles change as a function of pressure (or temperature). This can be achieved in one of two major ways: most simplistic is the application of empirical rules for how the hard sphere sizes compress with increasing pressure or temperature. This class of method was extremely popular for many years due to its computational simplicity and resulted in many applications of the hard sphere model to simple liquids, and is also the approach taken by *Jing and Karato* (2011) to improve the accuracy of extensions to elevated pressures and temperatures. While simple to implement, this empirical method suffers from its lack of strong physical grounding, where the rules governing the compressibility of the hard spheres are fairly arbitrary and chosen only to match the generally observed trends in liquid behavior. They therefore rely on fitting liquid data and have only limited capability for extrapolation and interpolation in pressure–temperature–composition space.

It is strongly preferable to use a physically based perturbation method, which uses hard spheres as the reference system to which higher-order corrections are made. The physical phenomenon that slightly compressible hard spheres seek to represent is the gradual decrease of the minimum particle spacing experienced by liquid particles with compression. This behavior reflects the limits of the hard sphere model, which approximates the steep Fermi repulsive energy barrier for particles at small separation distances with a step-function, or infinitely sloped hard wall. Of course, such a rough approximation was only ever appropriate over a limited range of conditions. As temperature increases, the liquid particles gain thermal energy allowing them to “climb” further up the repulsive slope, shrinking the effective hard sphere size. Similarly, increasing pressure confines liquid particles into ever smaller regions, balancing the energy penalty associated with climbing the repulsive barrier as particle sizes shrink against the energy benefit resulting from the increased free volume available to each particle. For this reason, it is energetically advantageous to steadily reduce the hard sphere size of each particle with compression, as depicted by the shrinking hard spheres in the third panel of Figure 4.5. By altering particle size, the liquid is able to maintain large configurational entropies in spite of decreasing volume, which helps to offset its increasing internal energy. This trade-off between the internal energy (associated with the packing of liquid particles) and the free energy (associated with the dependence of configurational entropy on free volume) is at the core of the “variational method” for hard spheres, which seeks an optimum hard sphere size through total free energy minimization. We will discuss the details of this method below, but for now, it is important to recognize how it relates to the evolving structure and energetics of the liquids upon compression and heating.

As indicated in the previous section, the final and most important aspect of oxide melt structure for the purposes of understanding compression is the availability of a variety of different oxygen coordination states for each cation. In the last panel of Figure 4.5, we show a snapshot of a simple liquid that has two different coordination states available to it, a large low coordination state in black and a compact high coordination state in red. The liquid is free to populate these states in whatever manner minimizes the total free energy.

This results in low coordinations dominating at low pressures and high coordinations at high pressure, as depicted in the figure by the increased presence of red particles in the high-pressure state. Both the populations of coordination states, shown as red and black in the figure, and the effective particle sizes for each state respond to changes in pressure and temperature, seeking to minimize the total free energy.

At this point, we must briefly digress to discuss the issue of coordination number. Cations in crystalline solids exist in a small finite number of coordination environments depending on the crystal structure. Typically, these coordination states are thought of as being restricted to integer values, corresponding to the number of oxygens bonded to the cation. This is a sensible notion for "ideal" structures, in which all nearest-neighbor oxygens lie at equal distance from the central cation. Many crystal structures, however, contain cation sites that are highly distorted, where the nearest-neighbor oxygens lie at a discrete set of unequal distances, making it more difficult to define which oxygens are directly bonded to the cation and which are shared unequally with neighboring cations. This complication reveals the need to define the "effective coordination number", which gives higher coordination weight to nearer neighbors and less to more distant ones. While there are many possible definitions of effective coordination number, we use that put forward by *van Meel et al.* (2012), since it is straightforward, using a sensible solid-angle-based weighting scheme, and does a good job reflecting the differences between different distorted crystal structures. [2]

---

[2] A more commonly used definition was introduced by *Hoppe* (1979), who used an exponential averaging scheme to give greater weight to closer neighbors. *Hoppe* (1979) fully admitted that the form of the weighting scheme is fairly arbitrary, and can only be judged on its ability to recover the correct values for ideal structures while providing useful insight into more distorted ones. Accordingly, we have tested this scheme against the more recent one by *van Meel et al.* (2012), and have found *van Meel et al.* (2012) to return more sensible values. Additionally, this new method results in coordination weights that are constrained to values less than

Like distorted solids, liquids also place cations inside geometrically non-ideal sites. While we depicted only two coordination states in Figure 4.5 for the purposes of clarity, liquids actually contains a spectrum of local coordination environments. Released from the constraints of periodicity, the distances and angles between cations and oxygens in liquids are dynamically evolving, causing the nearest-neighbor oxygens to sample a *continuous* distribution of bond distances, further emphasizing the need to consider fractional coordination states. While the concept of fractional coordination may be unfamiliar to many, it is crucial to understanding the structure and resulting thermodynamics of silicate and oxide melts.

Using this qualitative picture of liquid structure and thermodynamics as our guide, we are now prepared to consider the development of a quantitative model that captures these important behaviors.

4.3.2 Perturbing the Hard Sphere Mixture Model

Unlike dynamical models, such as first-principles molecular dynamics, which seek to directly simulate the motions of particles in a system, statistical mechanical models only attempt to represent the behaviors of a system probabilistically. The advantages to this alternative approach are that it produces models that are *many* orders of magnitude faster—the difference between desktop computers and super-computers, minutes and months of calculation time—and it also leads to models that are inherently scale independent, and so they do not suffer from simulation size or evolution time effects.

---

or equal to one for each neighboring particle, whereas the method of *Hoppe* (1979) frequently gives weights considerably greater than one for close-by neighbors. We find this to be fairly unphysical, since an atom cannot be said to have a bonding weight of more than 100%.

At the root of statistical mechanics is the recognition that each macroscopic state of the system, described by the state variables of volume, temperature, and composition, actually corresponds to a huge number of combined microscopic states. A macroscopic system (with of order at least Avogadro's number $\sim 10^{24}$ of particles) can only be completely described by its microscopic configuration, a list of the position and velocity vectors for every particle at every time step. Clearly, a "macroscopic dynamical model" would require an impossible amount of computing power. Instead, statistical mechanical models consider the range of available microstates, and assign relative populations to these states according to the rules of thermodynamics. For a closed system at constant temperature T, volume V, and composition $\vec{X}$, the second law of thermodynamics states that the system will achieve equilibrium when its Helmholtz free energy F is minimized, which is given by the sum of independent contributions $F = \sum F_i = \sum(E_i - TS_i)$, where E is the internal energy and S is the entropy. Therefore, the microstates of the system are populated in such a way as to minimize the total free energy. [3] This provides us with a simple recipe for constructing a statistical mechanical model, where we need only write down an expression for the free energy and minimize it.

Using the hard sphere mixture model as a guide, we can think of silicate and oxide melts as a collection of coordination-specific hard spheres, where each sphere represents a particular oxygen bonding environment about a cation lying at its center. By explicitly considering the range of available coordination states, we are able to capture how the contribution of each cation to the overall liquid structure depends on the oxygen coordination

---

[3] The simplest example of this is the familiar Boltzmann distribution, which describes the population of a set of independent states with different energy levels.

number, which controls the local connectivity between the cations. Given this physical picture, we have developed the **C**oordinated **HA**rd **S**phere **M**odel (CHASM), which applies a perturbation to the standard hard sphere mixture by both accounting for multiple coordination states for each oxide component and estimating how the average liquid structure affects the internal energy of the liquid. The total free energy of the CHASM liquid can thus be divided into its major components:

$$F_{\text{Tot}} \approx F_{\text{ideal}} + \Delta F_{\text{HS}} + E_{\text{struc}} + F_{\text{internal}} \tag{4.6}$$

where F_{ideal} is the ideal gas contribution, ΔF_{HS} is the configurational free energy contribution as calculated by the hard sphere mixture model, E_{struc} is the dependence of the internal energy on the average liquid structure, and F_{internal} captures the additional free energy contribution caused by the internal degrees of freedom available to each hard sphere particle, primarily associated with the freedom of movement of the bonded oxygens. Given the dependencies of each term, the total free energy can be written:

$$F_{\text{Tot}} = F_{\text{Tot}}(V, T, \vec{X}, \mathbf{p_{cn}}, \mathbf{d_{cn}}) \tag{4.7}$$

where the free energy is a function of the thermodynamic state variables $(V, T, \vec{X})$, as well as the model parameters describing the hard sphere attributes $(\mathbf{d_{cn}}, \mathbf{p_{cn}})$, which are the diameters and populations of the hard spheres as a function of coordination number for each oxide component of the liquid.[4] We now give a brief description of each term in

---

[4] The coordination populations are defined separately for each component such that $\mathbf{p_{cn}}_{ij}$ gives the fraction of cations of type i that are in coordination state j and therefore $\sum_j \mathbf{p_{cn}}_{ij} = 1$ for each component.

the total free energy expression. While, for the purpose of clarity, we save most of the details for the Appendix, it is important to recognize that all terms can be evaluated using a combination of straightforward analytic expressions and simple 1-D numerical integrals.

The first term in the free energy captures the contribution associated with a mixture of ideal gases. This captures the momentum carried by each particle, given by the standard expression for a single component ideal gas $F_{\text{id-gas}}$, combined with the ideal entropy of mixing for completely randomized particles $S_{\text{id-mix}}$:

$$\begin{aligned} F_{\text{ideal}} &= \sum_i X_i F_{\text{id-gas}}(V, T, m_i) - T S_{\text{id-mix}} \\ S_{\text{id-mix}} &= -k_B \sum_{i,j} x_{ij} \log x_{ij} \qquad \text{(where} \quad x_{ij} \equiv X_i \mathbf{p_{cn}}_{ij}) \end{aligned} \tag{4.8}$$

Note that these contributions are evaluated for the hard sphere particles rather than the individual atoms, and thus m_i and X_i are the mass and mole fraction of each oxide component (in a per cation basis). The mole fraction of oxide component i in the j^{th} coordination state is given by x_{ij}, which is equal to the relative population of that coordination state times the absolute abundance of that component. The occupation of multiple local coordination states leads to a significant increase in the entropy of mixing for liquids, reflecting the increase in the number of distinguishable randomized microstates. This fact is well known, and was found to adequately explain the high entropy of mixing observed across the MgO-SiO_2 binary in FPMD calculations (*de Koker et al.*, 2013).

The next term in the free energy is the adjustment resulting from a mixture of hard spheres. This analytic equation was derived using an approximate solution for the radial distribution function, referred to as the Percus-Yevick equation, and was first extended to hard sphere mixtures by *Lebowitz* (1964). Subsequent work improved the approximation (*Mansoori et al.*, 1971), yielding an expression that can be thought of as a standard black box for calculating the free energy of hard sphere mixtures. While this expression is shown in its entirety in Appendix 4.A, we note here that it takes the form:

$$\Delta F_{\mathrm{HS}} = kT \times f_{\mathrm{HS}}(V, \vec{X}, \mathbf{p_{cn}}, \mathbf{d_{cn}}) \tag{4.9}$$

where the free energy difference is a purely geometric function of the volume, hard sphere sizes and populations. The dependence on temperature is only as a multiplicative prefactor, in effect setting the overall energy scale. Together, the ideal and hard sphere terms represent the pieces of the standard hard sphere mixture model.

While generally useful, the standard hard sphere model lacks any contributions to the internal energy, which are crucial for describing large degrees of compression. As presented in Figure 4.5 and in the subsequent discussion, there exists a trade-off between the configurational free energy (captured by the hard sphere model) and the internal energy cost associated with the average liquid structure. This balance enables the particles to adjust their effective sizes to respond to changes in volume or temperature in order to maintain the minimum free energy. We therefore need an expression for the energy cost associated with a particular liquid structure. The simplest possible approach is to approximate the total structural energy as resulting from the sum over pairwise interactions—through an effective "pair potential" E_{pair}—of every particle with every other particle. This is achieved by considering interactions between a central reference particle of type c and the surrounding particles of type s:

$$E^{cs}_{\text{struc}} = \frac{1}{2} x_c \int_0^{\infty} E^{cs}_{\text{pair}}(r) \operatorname{Pr}^{cs}(r) dr \qquad \text{and} \qquad E_{\text{struc}} = \sum_{c,s} E^{cs}_{\text{struc}} \tag{4.10}$$

where the total energy is given by integrating the probability-weighted energy cost ($\operatorname{Pr} \times E_{\text{pair}}$), which depends on the separation distance r, over all possible separation distances. Additionally, x_c, the mole fraction of c particles, gives the probability of choosing a c particle at random, and the factor of $\frac{1}{2}$ exists to prevent double counting (since each particle is counted once as the central particle, c, and once as the surrounding particle, s). This expression is then evaluated for every possible pairing of distinguishable particles and summed over, cycling through each coordination state for every component.

The probability of finding particles at each distance is tied directly to the structure of the liquid through the radial distribution function $g(r)$, and thus we can rewrite the above equation:

$$\begin{aligned} E^{cs}_{\text{struc}} =& \frac{1}{2} V \rho_c \int_0^{\infty} E^{cs}_{\text{pair}}(r) 4\pi r^2 \rho_s g_{cs}(r) dr \\ =& 2\pi V \rho_c \rho_s \int_0^{\infty} r^2 E^{cs}_{\text{pair}}(r) g_{cs}(r) dr \end{aligned} \tag{4.11}$$

where the number densities of the central and surrounding particles are given by ρ_c and ρ_s. The key point is that the approximate RDF for the liquid is a direct output of the hard sphere mixture model, and therefore we need only impose a reasonable pair potential in order to calculate the structural perturbation. Determining the empirical pair potentials for the coordinated hard spheres is therefore at the heart of applying the CHASM method and requires significant attention. We defer that discussion until Section 4.3.3, where we detail how to determine liquid-appropriate pair potentials solely from data on the solid structures. For the meantime, we assume that such a determination has been made and that Equations (4.10) and (4.11) can be evaluated.

Finally we come to the last term in the free energy expression, which captures the effects of the internal degrees of freedom of each hard sphere particle. Thus far, every term has relied entirely on thinking of the hard spheres as indivisible particles—at this point we consider corrections that account for the limitations of this description. Each particle is composed of a central cation surrounded by a set of coordinated oxygens that are shared between neighboring particles. The oxide particle picture reflects how much cations and oxygens resist separating from one another, but it ignores the freedom of independent motion that the oxygens retain. We thus split the internal free energy contribution into its two major parts:

$$F_{\text{internal}} \approx F_{\text{bond ang}} + F_{\text{bond len}} = F_{\text{internal}}(V, \vec{X}, \mathbf{p_{cn}}) \tag{4.12}$$

where $F_{\text{bond ang}}$ expresses the free energy resulting from the positional freedom that is coupled with bond-angle distortion, and $F_{\text{bond len}}$ expresses the contribution due to the variability in bond length about the average value.

We have derived an expression for the first term in Equation (4.12), using elementary quantum mechanics, but to avoid distraction, we relegate that derivation to Appendix 4.D. The results show that the bond-angle freedom term relates to the cation-oxygen bond length, which is unsurprising since the oxygens can be thought of as lying on the surface of a “bonding sphere” with radius equal to the bond length. Most of the extra dynamics relate to motions of the oxygens along the surface of this sphere. There must, of course, be some motion of the oxygens along the radial direction causing bond length distortions, as represented by the second term in Equation 4.12, though we currently neglect any contributions from motion of this type. As we show in the next section, we can empirically relate oxygen bond length for a particular cation to the overall volume by examining a variety of solid structures. Additionally, the coordination number directly controls how many oxygens lie on the surface of the bonding sphere, determining the typical bond angles, and thus the coordination populations are also important to calculating the contribution from internal degrees of freedom. Notice, however, that there is no direct dependence upon either hard sphere sizes or temperature, as indicated by the right-hand side of Equation (4.12).

By combining the equations above with those in Appendix 4.A-4.D, we now have the ability to evaluate the total CHASM free energy. This relies specifically on providing the coordinated hard sphere pair potentials, which is discussed in detail in the next section. As alluded to previously, the final step is to apply the principle of energy minimization:

$$F_{\mathrm{liq}}(V, T, \vec{X}) = \min_{\mathbf{p_{cn}}, \mathbf{d_{cn}}} \{F_{\mathrm{Tot}}\} \tag{4.13}$$

where the state of the system is that which minimizes the total free energy. Thus, for a particular set of state variables V, T, and $\vec{X}$, we can obtain self-consistent thermodynamically derived values by minimizing the total free energy with respect to the hard sphere parameters. This generic method of determining the model-dependent parameters is also called the "variational method" for hard spheres, due to its connections to the calculus of variations[5], and was developed by *Mansoori and Canfield* (1969). In that and subsequent works, the authors developed improvements to the description of compositional hard sphere mixtures, but remained limited to any considering the added effect of liquid structure. We have thus extended the same technique to directly tracking the evolution of coordination state. To simplify and speed up calculations, the dependence of the hard sphere sizes and populations on coordination number can be parameterized with simple smooth functions, thereby enforcing the expected systematic behavior while also reducing the number of parameters that must be varied (details are presented in Section 4.3.4). Because all of the expressions involved in evaluating the total free energy are either analytic or simple 1D numerical integrals, evaluating the free energy is a trivially fast operation, taking less than a second on a modern personal computer. We are therefore able to use a standard numerical minimization routine in MATLAB, allowing the solution for each state point to be calculated in only a few minutes, in contrast to the weeks or months necessary on multiprocessor machines in dynamical simulations.

4.3.3 Training Pair Potentials on Solid Structures

Now that we have presented the general framework of the CHASM approach, we will discuss the details of how to obtain reasonable values for the pair potentials by training on the equations of state of solid polymorphs. This step is critical, since the pair potentials represent the primary input to this model, determining the structural energy perturbation

---

[5] The liquid free energy in equilibrium can be thought of as a functional of the total free energy, which is subject to a minimization constraint. We imagine using a series of trial expressions for the free energy, and vary the hard sphere parameters until the minimum energy state is achieved.

that is at the heart of the variational method. Additionally, we must also determine the relationship between oxygen bond length and volume, which is provided by the empirical trends apparent in the solid crystal structure data. While bond lengths are not an explicit part of the general CHASM framework—since oxygens are only represented in terms of coordination number—they are required to estimate the bond-angle correction to the free energy.

As discussed at length in the previous section, liquids populate a continuous spectrum of local atomic structures, while crystalline solids are restricted to the small subset that are both periodic and minimal energy configurations. Though the range of available options is much narrower, differently structured crystals of constant composition (called crystal polymorphs) can be thought of as discretely sampling the same continuum that is available to the less highly-constrained liquids. This implies that we can gain considerable insight into the energetics of particular atomic arrangements by studying the solid structures. Ideally, we would have a computational tool that could rapidly determine the internal energy of any arbitrary ionic arrangement, but such a tool would need to solve Schrödinger's equation and therefore require first-principles methods like density functional theory, which are inherently both iterative and extremely computationally intensive. Instead, we look to the well-studied energetics of the solid structures to develop a set of empirical pair potentials that can approximately capture the dependence of internal energy on atomic configuration. When applied to the atoms themselves, this strategy represents a fairly standard approach for determining potential functions that can be used in empirical molecular dynamics simulations. Though we are not performing MD simulations, we do benefit from the general knowledge such studies provide about the features and limitations of pair potentials.

Empirical potentials represent the internal energy as a sum over either pairwise or many-body particle interactions using a suitably flexible and simple functional form. The most well-known example is the Lennard-Jones potential, which is appropriate when weak van der Waals attractive forces dominate at large separation distances: $E_{LJ}(r) = 4\epsilon[(\sigma/r)^{12} - (\sigma/r)^{6}]$, where ϵ and σ are the energy and distance scales. A more flexible potential form is given by the generalized Morse potential, which represents the repulsive and attractive parts using exponential decay functions:

$$E_{\text{exp-exp}}(r) \approx \epsilon_R \exp\left(-\frac{r}{\sigma_R}\right) - \epsilon_A \exp\left(-\frac{r}{\sigma_A}\right) \tag{4.14}$$

where ϵ_R & ϵ_A are the energy scales and σ_R & σ_A are the length scales for repulsion and attraction, respectively. In order to remain physical, with an asymmetric energy well that has a steep repulsive barrier at short distances, the parameters must take values with $\epsilon_R >> \epsilon_A$ and $\sigma_R < \sigma_A$. When applied to ionic particles, it is also necessary to add a Coulombic term to the interaction energy. While functions of this type are loosely motivated by physical considerations, they can only be expected to capture the observed energetic variation over a limited range of conditions. Accordingly, it is common to develop pair potentials that are appropriate for small deviations from a particular configurational environment, such as atomic vibrations within a particular crystal structure.

In order to extend the suitability of the potentials, it is usually necessary to add more and more corrective terms, which add angular dependence for dipole fields, impose bond-angle restrictions, or account for 3-body interactions, significantly reducing the simplicity of the approach and increasing the care required for obtaining reasonable parameter values. The most common downside to using pairwise-only atomic potentials, like Equation (4.14), arises from the fact that such expressions are forced to represent total bonding energies as strictly proportional to coordination number, since each bond contributes the same energetic weight. This tends to impose an unrealistic preference for high coordination numbers, since the total energy can be lowered by surrounding each cation with as many oxygens as possible. In reality, there is an increasing cost to placing more particles in a confined area, caused by the increase in local electron density (*Daw et al.*, 1993). Each subsequent particle actually sees a reduced energy benefit for bonding, compelling the ions to adopt less extreme coordination numbers.[6]

It is important to recognize that our goal is quite different from MD studies—we are not seeking to directly model the individual positions of cations and oxygens. Instead, we need only capture the average relative placement of effective hard sphere particles, which represent the basic structural units from which each liquid or crystal configuration is built. This simplification affords significant advantages over the standard pair potential approach by sidestepping the issue of suitability. Rather than developing complicated atomic potentials that are capable of representing vastly different local configurations, we instead restrict ourselves to only representing the interactions of hard sphere particles that are inherently coordination specific. By imposing the constraint that the pair potential values must be smooth and slowly varying functions of coordination number, we ensure that the

---

[6] The embedded atom method is a very successful many-body potential theory which accounts for this effect when directional bonding remains unimportant (*Daw and Baskes*, 1984; *Daw et al.*, 1993), though there is a significant added cost in terms of both complexity and the number of additional parameters whose values must be determined in order to apply the technique.

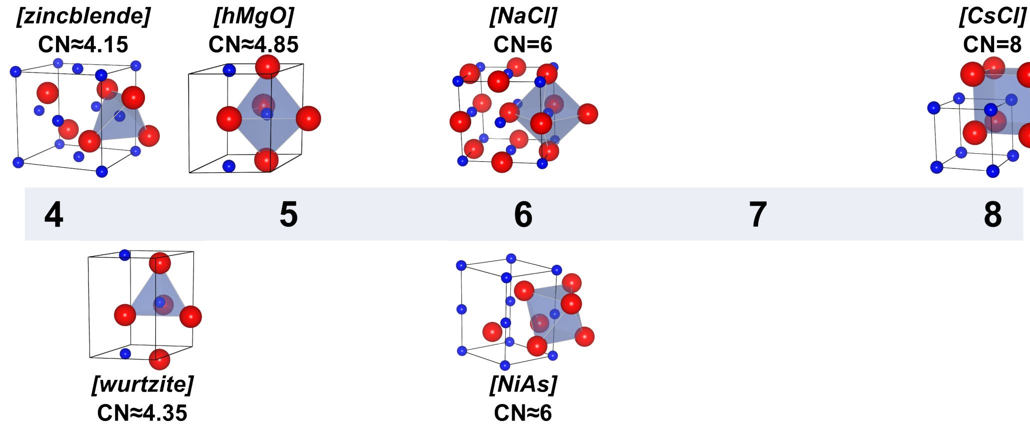

Figure 4.6: Representation of the unit cell structures and oxygen coordination polyhedra for the six theoretically realizable polymorphs of MgO. Each structure is displayed along an axis representing the effective coordination number. In reality, only the NaCl structure (periclase) is stable under terrestrial conditions. Nevertheless, the other structures are theoretically possible and can provide great insight into the energetics of oxygen-coordinated Mg.

resulting potentials are well behaved and improve the interpolation behavior of the derived potentials. This is particularly important since the solid polymorphs only sample a small set of coordination states and thus reasonable interpolation properties are an absolute requirement of potentials that are used for liquid calculations. Most importantly, as the local coordination is a prescribed attribute of each particle rather than a derived quantity based on model output, we no longer suffer from the common issue of improperly favoring high oxygen coordination states. Additionally, since each particle is neutrally charged, there is no need for additional Coulomb terms. By specifying pair potentials for the effective particles, rather than the atoms themselves, we are able to retain a simple functional form, as in Equation (4.14), without sacrificing the flexibility necessary to represent the changing nature of atomic interactions that results from evolving coordination states.

Having motivated and developed a general strategy for representing hard sphere potentials, we now demonstrate how to train the potential parameter values using equation of state data for the MgO polymorphs. MgO is chosen because it represents the simplest possible oxide and yet is extremely important to our understanding of the Earth. In the pressure range experienced in the silicate Earth, pure MgO exists only as the mineral periclase, which has the B1 or NaCl "rock-salt" structure, with an oxygen coordination number of 6. Depending on the packing efficiency of the unit cell, MgO could potentially adopt a range of structures, which are shown in Figure 4.6 ordered along an effective oxygen coordination line. This figure indicates the range of periodic structural options available MgO and other "AB" crystals, including CsCl, ZnS, ZnO, CaO, and BN. Whether a particular chemical system will actually adopt a given structure depends on the energetics of that configuration as dictated by quantum mechanics. So stable is the NaCl structure for MgO that density functional theory calculations have placed the pressure-induced phase transition to the denser CsCl (or B2) structure at somewhere between 400 and 500 GPa (*Karki*, 1997; *Jaffe et al.*, 2000; *Joshi et al.*, 2012). Looking to other analog AB crystal systems, we know that MgO should be able to theoretically adopt the low coordination zinc-blende (B3) and wurtzite (B4) structures, though at unrealizable "negative pressures". Though no structures other than NaCl have ever been observed for MgO in the lab, there are numerous studies that have examined both the high and low (negative) pressure polymorphs using density functional theory (see, for example, *Karki et al.* (2007); *Joshi et al.* (2012); *Jaffe et al.* (2000); *Oganov and Dorogokupets* (2003)). These studies provide energy-volume curves, which when coupled with known atomic positions, can form the basis of a training dataset for simple coordinated pair potentials.

For training our MgO pair potentials, we rely on the dataset produced by *Joshi et al.*

(2012), as it examined all six of the available structures shown in Figure 4.6. The fact that all energy curves were calculated self-consistently within a single study is important, since each study necessarily introduces an arbitrary energy offset parameter By using a self-consistent training set, we need only allow for a single global offset term, rather than one for each study which could amplify degeneracies in the fitted parameters. The calculated equations of state from *Joshi et al.* (2012) for the six theoretical structures of MgO are shown in Figure 4.8. In addition to the four previously mentioned structures, these also include two non-ideal distorted structures: the NiAs structure is six coordinated like periclase, but has a highly inefficient packing scheme for the cations resulting in large distortions of the nearest-neighbor cation distances, while the hMgO structure is a buckled boro-nitride variant that provides nearly 5-coordination for the cations. Together, these six structures with their computed effective coordination numbers and relative cation positions provide sufficient information to train the coordination-dependent pair potentials.

In order to obtain a simple parameterization that describes the total internal energy of each atomic configuration in terms of the pairwise interactions of cations alone, we must first select a form for the pair potential. The attributes of the pair potential are assumed to vary systematically with coordination number, thereby providing a simple way to capture how local bonding environment in turn affects the energy. For both its familiarity and flexibility, we choose the generalized Morse potential, which can be described most simply as the difference of two exponential decay functions (see Equation 4.14). While this parameterization has the simplest mathematical form, it is not very useful for fitting. The potential

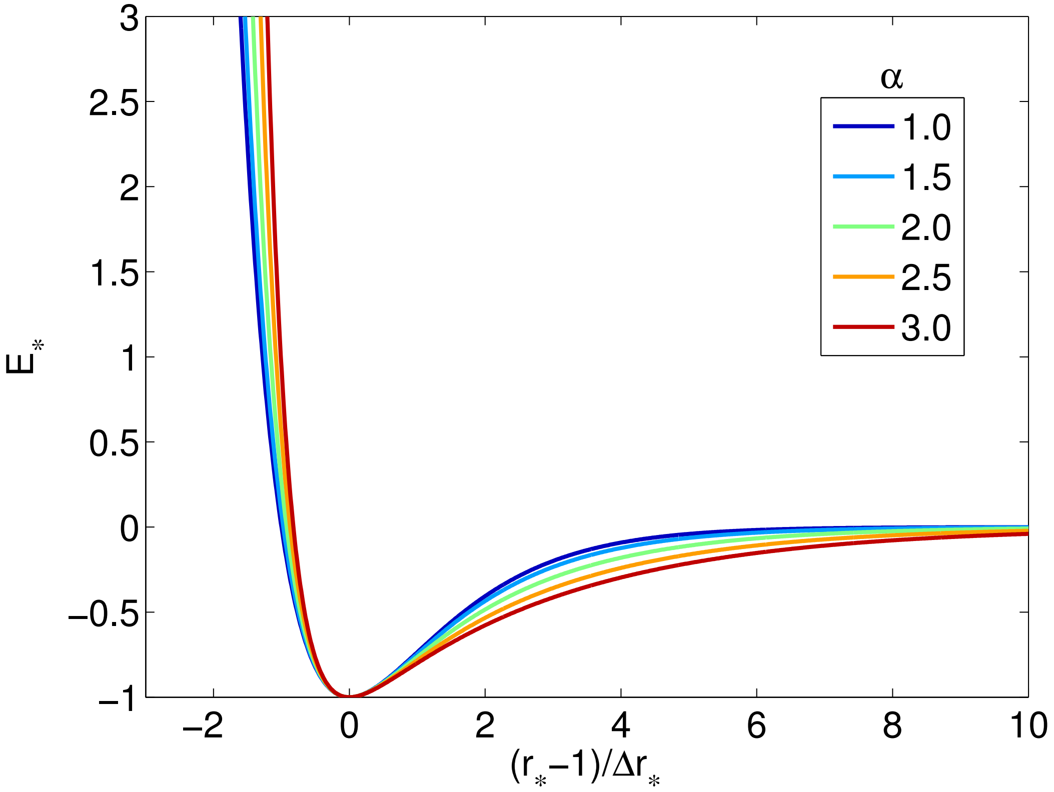

Figure 4.7: Normalized plot of the Generalized Morse Potential. The axes are chosen to force all wells to overplot one another. The only remaining degree of freedom is the shape parameter α. We choose to fix its value to $\alpha = \sqrt{2}$, which corresponds to the standard Morse Potential form, in order to prevent over-fitting.

is thus recast into the following "normalized Morse potential" form, depicted in Figure 4.7:

$$\begin{aligned} E^*_{\text{pair}}(r^*) =& \frac{1}{\alpha^2-1}\left\{\exp\left[-\alpha\frac{(r^*-1)}{\Delta r^*}\right] - \alpha^2 \exp\left[-\frac{1}{\alpha}\frac{(r^*-1)}{\Delta r^*}\right]\right\} \\ &\text{with,} \qquad E^* = E/E_D \quad \text{and} \quad r^* = r/r_e \end{aligned} \tag{4.15}$$

where the energy and length scales defining the depth and position of the energy well are given by E_D and r_e, and the relative width of the energy well is defined by Δr^*. Together, these 3 parameters scale the position and dimensions of the energy well, as depicted in Figure 4.7. Lastly, the overall shape of the well is given by the value of α, which primarily controls the curvature of the distant half of the well as shown in Figure 4.7. This parameterization, equivalent to Equation 4.14 with 4 free parameters, can be reduced to the standard Morse potential by fixing $\alpha = \sqrt{2}$. While fixing α removes flexibility from the function, we employ this strategy to avoid overfitting since the six compression curves do not sample a sufficient variety of cation distances to independently constrain the precise well shape.

The fitting procedure itself is fairly straightforward. First the atomic positions for the periodic crystals are calculated up to some large cutoff radius, which is many times larger than the nearest-neighbor cation distance. Then the total pairwise interaction energy is determined by evaluating Equation 4.15 at each separation distance and summing over all cation pairs. Finally, we also include a "tail correction", which roughly accounts for the effect of truncating the sum at a finite cutoff radius. The form of this correction term is exactly the same as Equation 4.11, where beyond the cutoff radius, we neglect the effect of small fluctuations in particle density setting $g_{cs}(r > r_{\text{cut}}) = 1$. This results in a trivial exponential integral for the Morse potential that is performed analytically.[7]

In addition to the direct interaction energy reflecting the positions of each cation, we must introduce a correction to account for the strong distortions present in some of the structures like NiAs and hMgO. This correction counteracts the excessive repulsive energies predicted by the pair potential in the case of distorted closely-spaced cations. The pair potentials are designed to capture the general energetic dependence of coordinated cations, and can therefore be thought of as describing the energy cost of "ideal" atomic arrangements. Distorted structures, however, have the freedom to rotate oxygen positions to move them out of the way and make room for the closely spaced cations, thereby reducing the effective energy cost of such an arrangement. This effect depends almost exclusively on the separation distances of the nearest-neighbor cation pairs, which induce the largest repulsive energies. To account for this difference, we apply a simple additive corrective term based on the concept of the effective coordination number:

$$\Delta E_{\text{corr}} = -\sum_i w_i (E_{\text{pair}}(d_i) - E_{\text{pair}}(d_{\text{eff}})) \tag{4.16}$$

where w_i is the coordination weight of the i^{th} nearest-neighbor cation and d_{eff} is the effective cation separation distance considering all neighboring cations, both calculated using the method of *van Meel et al.* (2012). Applying this expression to each cation, we can imagine that we are determining the energy impact of moving all of the nearest-neighbor cations from their actual positions to their average effective separation distance, which are more reflective of the energetic cost of the atomic arrangement. This corrective term is only

---

[7] The inclusion of this tail correction causes the total pairwise energy to converge much more rapidly, enabling smaller values of the cutoff radius.

important for distorted structures like NiAs, where it is large and negative. For ideal atomic arrangements, the actual and effective distances are equal, and thus the correction term is zero.

Using the calculation outlined above, we can calculate a model energy compression curve for any chosen set of pair potential parameters r_e, E_D, and Δr^* (where $\alpha = \sqrt{2}$ is fixed in this case to avoid overfitting). Since each parameter represents a scale factor that could potentially vary over orders of magnitude and is constrained to be positive, we use $\log r_e$, $\log E_D$ and $\log \Delta r^*$ as our fitting parameters. Each compression curve is first fit individually. Since we seek a model that merely captures the general behavior of coordinated cations, it is not to important assign error bars to each measurement as we know that inadequacies of the model, not errors in the DFT data, will dominate the residuals. Therefore we apply the standard method of unweighted least-squares regression. In this case, the goodness of fit is described in terms of the explained fraction of the variance or $R^2 = 1 - \mathrm{Var}(E_{\text{resid}})/\mathrm{Var}(E_{\text{data}})$, with a value of 1 corresponding to a "perfect" fit. After fitting each curve individually, we construct a global model that enforces smooth dependence on coordination by asserting that each potential parameters is described by a low-order polynomial in coordination number. To get an initial guess to the final global model, we fit the individual best-fit parameters with a quadratic, after which the entire collection of energy-volume curves are fit jointly. The final results of this global fit are shown in Figures 4.8 and 4.9. As seen in Figure 4.8, the general quality of the fit reasonably good with $R^2 = 0.986$. The largest residuals belong to the two highly distorted structures, NiAs and hMgO, where the corrective term given by Equation 4.16 is able to account for

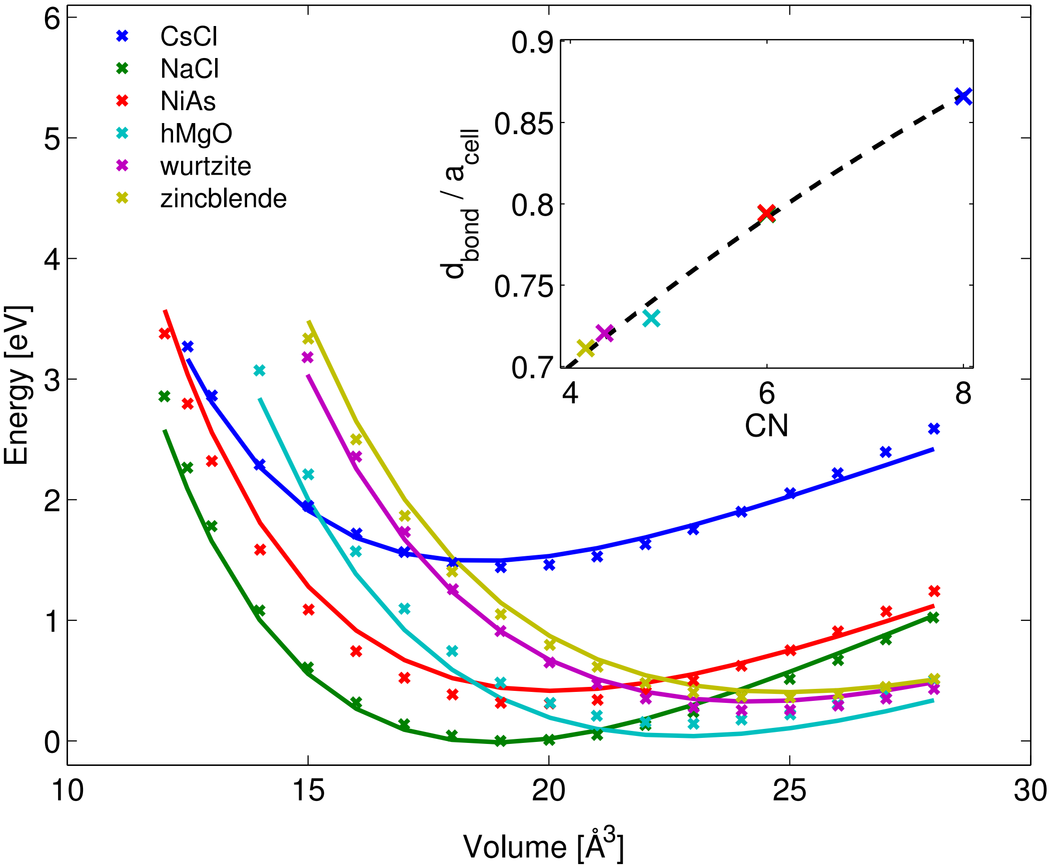

Figure 4.8: The first-principles energy-volume curves for the six polymorphs of MgO (*Joshi et al.*, 2012), are plotted together with the results of the global fit for the coordinated pair potentials. This fit assumed quadratic dependence of the three Morse potential scale parameters on coordination number, and kept the shape parameter fixed to $\alpha = \sqrt{2}$, the value corresponding to the standard Morse potential. Thus, using 9 free parameters, we obtain a good fit to the data with a goodness of fit (explained fraction of the variance) of $R^2 = 0.986$. Residuals are higher for more distorted structures, like NiAs and hMgO, as expected. The inset shows the smooth dependence of the oxygen bond–length scale ratio on coordination number, and is fit with a quadratic. This dependence is only important as a higher order correction to the free energy, in terms of the bond-angle contribution.

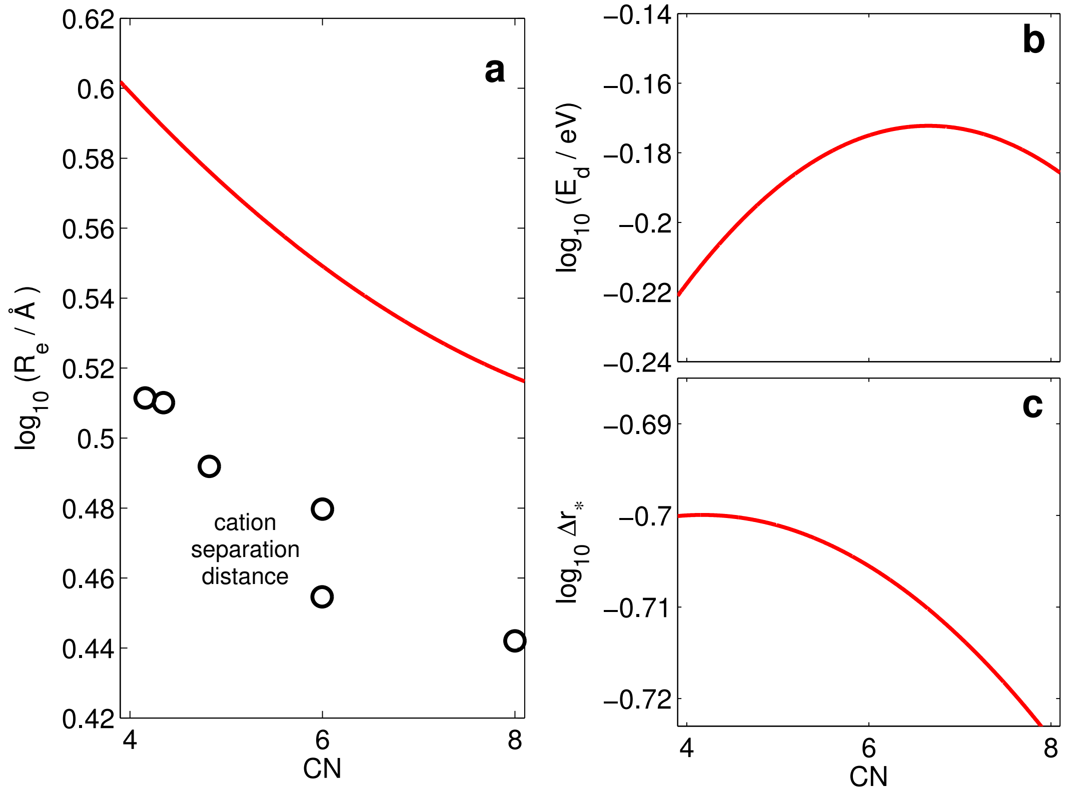

Figure 4.9: The best-fit trends for the pair potential scale parameters are plotted against coordination number. These trends correspond to the global best fit, shown in Figure 4.8. Panel (a) shows the variation of the equilibrium radius, (b) shows the energy well depth, and (c) shows the width of the energy well. Also plotted in panel (a) is the cation separation distances for each crystal structure at ambient pressure. The relationship between them and the equilibrium radius can plainly be seen, where the equilibrium radii are approximately given by scaling up the cation separation distance.

much, but not all, of the distortion effect. Also shown in the inset of Figure 4.8, is the systematic relationship between coordination number and the oxygen bond length in terms of the ratio of bond length to unit cell parameter, where $a_{\text{cell}} = V^{1/3}$. This nearly linear trend reflects the ability to more efficiently pack space with higher coordination numbers. Approximate values for the oxygen bond length, given by the quadratic fit shown in Figure 4.8, are needed for evaluating the internal degrees of freedom term to the free energy, which reflects the added internal states of each hard sphere caused by the motions of the oxygens.

The polynomials corresponding to the global best fit are shown in Figure 4.9. In panel a, the systematic decrease in the equilibrium radius with increasing coordination is plainly seen. Also plotted are the effective nearest-neighbor cation distances for each structure at ambient pressure. It is unsurprising that the equilibrium distance is related to the actually observed separation distances, though they are larger by roughly 20%, reflecting the constraints that periodicity places on the atomic positions. Panels b and c show the variation of the energy well depth and width with coordination number. To visualize what these polynomials mean, Figure 4.10 shows the pair potential energy wells calculated for a range of coordination numbers. The systematic changes in the pair potential parameters has the effect of shifting the energy wells toward smaller radii with increasing coordination. The depths of the wells also vary, causing six-coordinated pairs to have the lowest equilibrium energy, related to the stability of the 6-coordinated periclase structure. From this figure, we can see that the lowest energy curve at each separation distance shifts from low to high coordination as the separation distance decreases. It is primarily this trend that induces the gradual evolution of coordination number in oxide liquids with increasing compression.

4.3.4 Determining Liquid Properties using CHASM

With the coordination-dependent pair potentials in hand, we are now ready to apply the CHASM to determine the average liquid structure and thermodynamics. In this section, we demonstrate how to use the free energy minimization framework, described in Section 4.3.2, to calculate the thermodynamic properties of oxide liquids, specifically applying them to the MgO system.

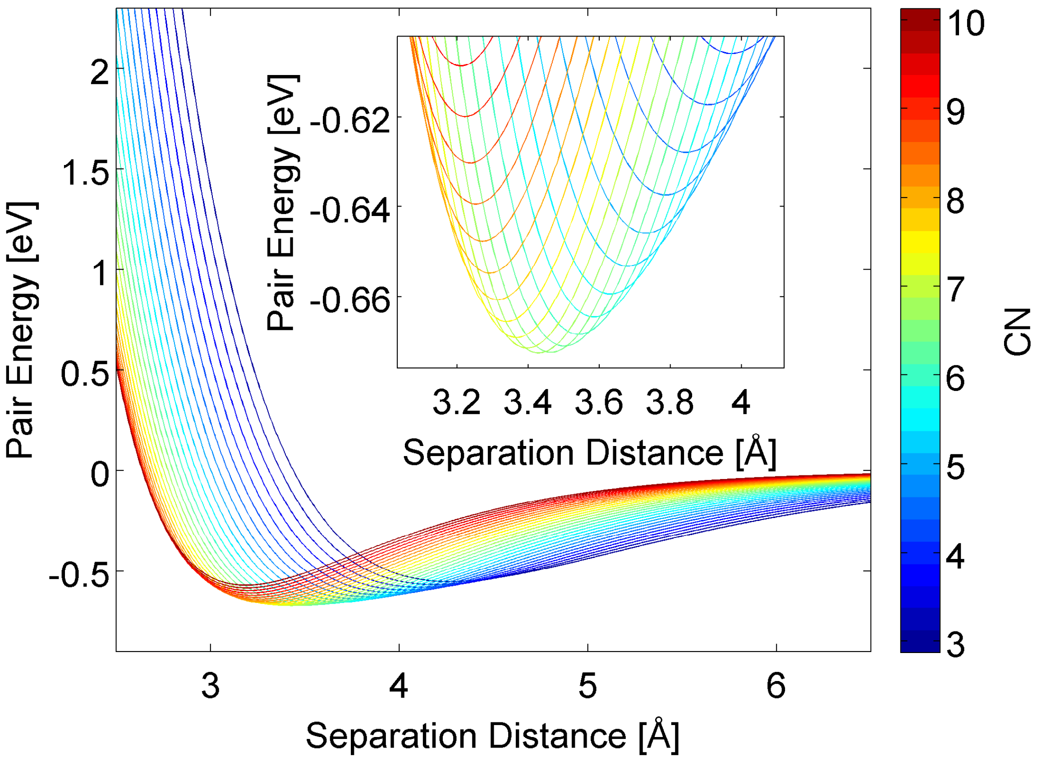

Figure 4.10: Results from the pair potential global fit, showing the energy well corresponding to each fractional coordination number along a continuum between 3 and 10. The inset figure shows a zoomed view of the minimum, which occurs for a coordination number near 6.

We begin by thinking of a complex coordinated liquid as being composed of an ideal mixture of liquids different oxygen coordination states. While this model neglects the interactions between different coordination states, which can play an important role in both the energy and entropy of the liquid, it represents a first order approximation to the liquid's properties. The variational method for hard spheres dictates that for a simple single component liquid, the correct value for the hard sphere size is simply the one that minimizes the free energy, represented by the sum of terms in Equation 4.6. The basic meaning of each term is described in Section 4.3.2 and the details of the calculation are given in the Appendix. The most important term to recall at this point is the structural energy perturbation term, which approximates the configurational internal energy using pair potentials. In the previous section, we developed a simple polynomial description of the pair potential terms as a function of coordination number, as shown in Figure 4.8. Using that model description, we obtain the pair potential parameters describing a range of coordination states, as shown in Fig. 4.10, for use in calculating the total free energy. It is important that coordination spectrum is sampled with sufficiently high resolution to adequately represent the continuous nature of coordination number for liquids. A sampling frequency of 0.25 coordination number is used in this study and deemed accurate based on the energetic differences between adjacent states as compared to kT.

At this point, we treat the total free energy function as a black box, which due to its primary reliance on analytic expressions, provides rapid function evaluations (each lasting only a fraction of a second). To determine the hard sphere size for each fixed coordination liquid, it is simply a matter of using standard function minimization routines[8]. At a range of

---

[8] The code developed in this investigation is implemented in MATLAB, and thus uses the library functions

sample volumes, the appropriate hard sphere size is thus determined for each coordination state along with the associated liquid free energy. The resulting set of free energy curves for the sampled coordination states of MgO are shown in Figure 4.11. Focusing on individual curves, each color-coded by their coordination state, we can see the overall trend that increasing coordination state simultaneously increases the zero-pressure free energy (shifting it upward), decreases the zero-pressure volume (shifting it left), and decreases the typical bulk modulus (reducing the curvature). This results in the expected behavior that the lowest energy coordination state changes gradually from low to high coordination as the liquid is compressed. Also shown in the inset of the same figure is the variation of the determined hard sphere diameters with compression. While this is an internal model variable that does not provide direct physical insight, we show it here to note that over much of the high compression region, the hard sphere sizes are nearly linear in log-volume. This supports the empirical deformability correction imposed by *Jing and Karato* (2011) to roughly account for compression effects. Unfortunately, there is non-negligible curvature at low pressures, and the shift of coordination states with compression will also induce added curvature. Nevertheless, this indicates that such a correction is not unreasonable for extending the applicability of the standard hard sphere model to slightly higher pressures.

After determining the compression behavior of independent coordination states, we obtain a rough first-order approximation of the liquid by treating each coordination as a quasi-independent state. Thinking of them as a set of non-interacting states that range in energy, Boltzmann's constants can be used to estimate the population distribution that minimizes the free energy: $p_i \propto \exp(-F_i)$, where F_i is the free energy and p_i is the pop-

---

fminunc and fminbnd, though any multidimensional nonlinear minimization routine should work.

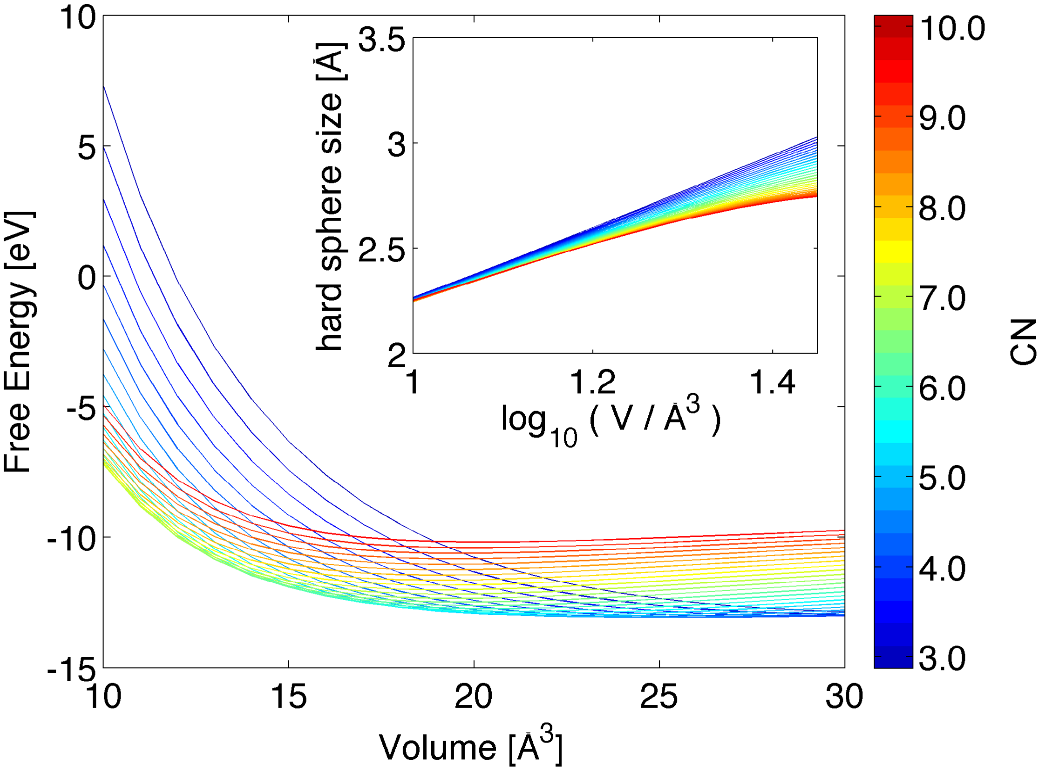

Figure 4.11: The free energy compression curves for a set of hypothetical MgO liquids each composed of a single fixed coordination number. An approximate set of coordination populations can be determined using Boltzmann factors at each volume. Thus, we can see that coordination state with the minimum free energy at a particular volume should lie near the peak of the coordination population distribution. The inset shows the variation of hard sphere sizes with increasing log-volume. The near linearity of these curves provides support for the empirical hard sphere deformability correction used in *Jing and Karato* (2011).

ulation of the i^{th} coordination state. This results in a population distribution that is a good initial guess for the true distribution, which accounts for interactions between the differently coordinated hard spheres. To enable the efficient calculation of the global free energy minimum, we parameterize the variations in population and hard sphere size, relying on low-order polynomials to capture smooth trends with a simple functional form. The hard sphere diameters are relatively straightforward, with a polynomial dependence of the diameter on log-coordination number capable of representing the observed variations with only a few degrees of freedom (3 to 5). The population distributions are somewhat trickier, adopting typical Gaussian-like peaks. To retain the flexibility afforded by polynomials, we model the log-population values as having polynomial dependence on coordination number; the choice of a second-order polynomial would restrict the model to a standard normal distribution (or Gaussian peak), which is not adequate to describe the observed shapes. We therefore choose a fourth-order polynomial, which is sufficient to capture the shapes of the initial population distributions over a range of volumes.[9]

Together, these parameterizations vastly reduce the size of phase space that must be searched to minimize the free energy, reducing the number of variables from over 50 to between 5 to 10, depending on the chosen polynomial degree. Given this simple parameterization, it is only a matter of using a standard minimization algorithm to locate the set of hard sphere size and population parameters that yields the lowest total free energies. We found that the best general procedure is to start by evaluating the hard sphere sizes (and free

---

[9] It should be mentioned that we restrict allowable solutions to those that result in only a single peak in the population distribution over the modeled coordination number range.. Therefore, only parameter combinations that result in monotonic increasing and decreasing behavior to the left and right of the peak are allowed. This condition is crucial to prevent unphysical minor peaks from appearing at either very high or very low coordination number, which occur as an artifact of trying to match the shape of the primary peak.

energies) individually for each coordination state. From there, the Boltzmann distribution is used to obtain a population estimate, which is represented using the polynomial formalism described above. Alternating between the two groups of parameters, fitting one set while the other remains fixed, appears to yield the most rapid convergence. In practice, we find that only a single additional iteration step is generally necessary to reach convergence for the free energy values. While the total free energy convergence fairly rapidly, after only tens to hundreds of function evaluations, the details of the populations distributions themselves can take more time, as seen by the fluctuations in the population curves in Figure 4.12.

Using the procedure described above, we calculate a set of isothermal compression curves over a range of temperatures and volumes. As stressed throughout the development of CHASM, obtaining the stable minimum free energy configuration is quite rapid requiring only a few minutes of time on a modern processor. Furthermore, each state point is entirely independent of the others, and thus the code can be run simultaneously on multiple processors if fine sampling of large compositional spaces is required. From the output of a set of equilibrium calculations, we can immediately examine the evolution of coordination number without any further processing. Figure 4.12 shows the evolution of the coordination state populations as a function of compression for MgO liquid at 3000K. In the main panel of the figure, the calculated populations of each coordination state are colored according to their relative probability values. From this figure, we can see the smooth evolution of the average coordination number with compression from values near 4 at 30 $\mathring{A}^3$ up to roughly 7.5 at 10 $\mathring{A}^3$, which is in strong agreement with the findings of the variation of average coordination number with compression presented by *Karki et al.* (2006). This plot also indicates the width of the distribution over coordinations states at a given volume. That width responds directly to temperature in a Boltzmann-like fashion, populating a wider range of more energetically costly states at higher temperatures. The inset to the same figure displays the same information in a different way, now showing the evolution of the occupation of each coordination state as a function of compression. For viewing purposes, we have binned the fractional coordination states together into integer width bins. When viewed in this way, we can highlight the contribution of each coordination state to the overall changing structure of the liquid. While *Karki et al.* (2006) does not show any plots like this tracking the distribution of coordination states, a later paper on silica (*Karki et al.*, 2007) does show the evolving populations of each coordination number, which shows the same qualitative behaviors as seen here, and are likely to be rather similar since the average coordination number are in agreement.

Finally, we can obtain the equation of state curves for a set of isotherms calculated using CHASM and compare with first-principles results. In Figure 4.13, we show the derived pressure-volume curves for a set of MgO liquid isotherms. The direct output of the CHASM are a set of free energy curves, which are generally of less interest to most people. In order to convert each curve into a pressure volume curve, we use the same strategy as that used by the FPMD practitioners (see, e.g., *de Koker and Stixrude*, 2009), which is simply to fit a finite strain equation of state to each isothermal curve. The finite strain model is also known as the Birch-Murnaghan equation of state. We find that a standard third-order model, with 4 parameters, V_0, F_0, K_0, and K_0' is perfectly adequate to represent the free energy

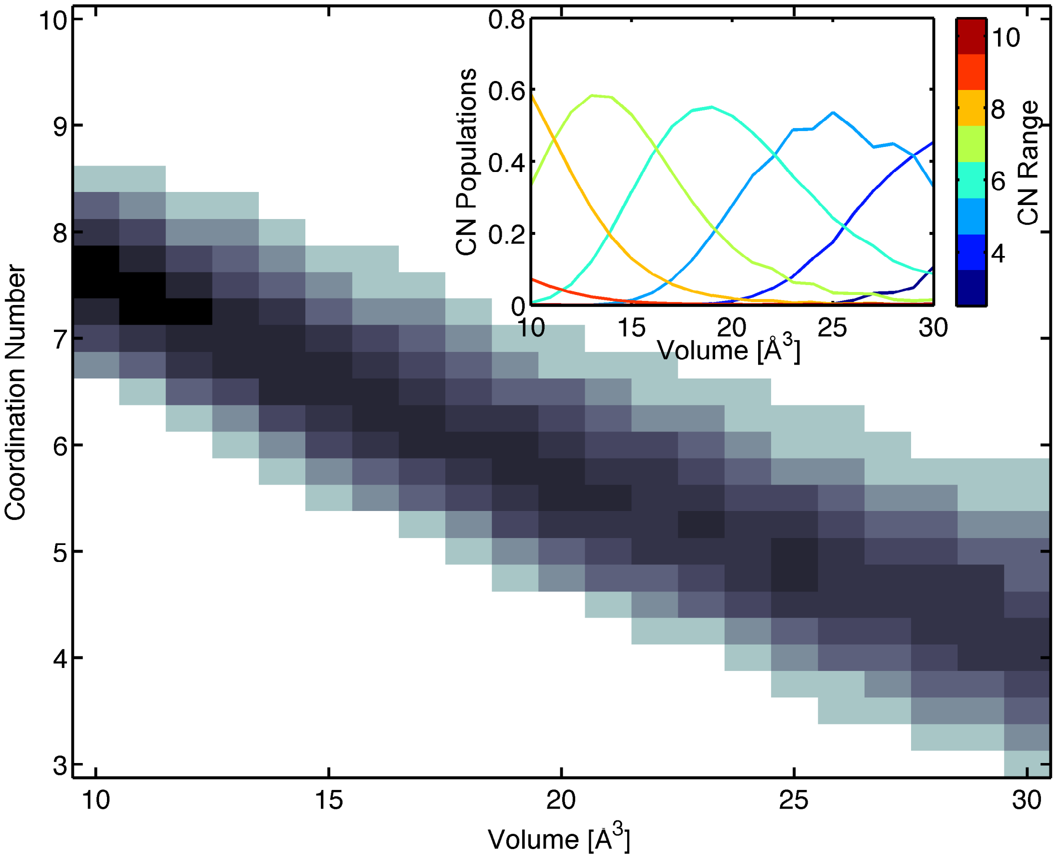

Figure 4.12: Evolution of the coordination populations for MgO liquid at 3000K. The main figure shows probability distribution, indicated by the darkness of the colormap, amongst the coordination states at each volume. The general trend of increasing coordination number with compression can be seen, as can a slight reduction in the width of the distribution with increasing compression. The inset figure shows binned coordination populations as a function of volume, showing dominantly 4-coordinated Mg transforming smoothly to dominantly 7 and 8-coordinated Mg at the highest pressures.

curves. Using this fit to each isotherm, it is then simple to calculate the pressure for a range of volumes, as shown in Figure 4.13. Also shown in the inset of the same figure is plot of the free energy curves against a normalized volume, V_X, which is taken to be the zero-pressure volume at 3000 K. We find a 3000K volume scale of $V_X = 25.4 \mathring{A}^3$, which falls short of the first-principles result of $V_X = 27.4 \mathring{A}^3$ (*Karki et al.*, 2006). In all likelihood, the fact that we are underestimating the zero-pressure volume is tied to some inadequacies in the internal degrees of freedom correction, probably related to the as-yet unaccounted for freedom of varying oxygen bond length. Nevertheless, if we plot the scaled free energy curves, we can see that we are doing quite an excellent job of matching the behavior in the first-principles calculations. This is our strongest indicator that the CHASM formalism is capable of accurately capturing the behavior of oxide melts.

4.4 Conclusions

We have developed a new simplified model to model the structure and thermodynamics of oxide and silicate melts. The **C**oordinated **HA**rd **S**phere **M**odel (CHASM) is based on an extension to the standard hard sphere mixture model which accounts for the range of local oxygen coordination state about each cation, which appears to be the key to compression mechanisms in oxide melts. In this formalism, a coordinated hard sphere is taken to represent a single cation surrounded by a bonded shell of coordinated oxygens, where the coordination number represents the local connectivity and bonding relations between each cation and its neighbors. The CHASM is based on the principle of free energy minimization, using it to determine sizes and populations of the hard sphere oxides. In this

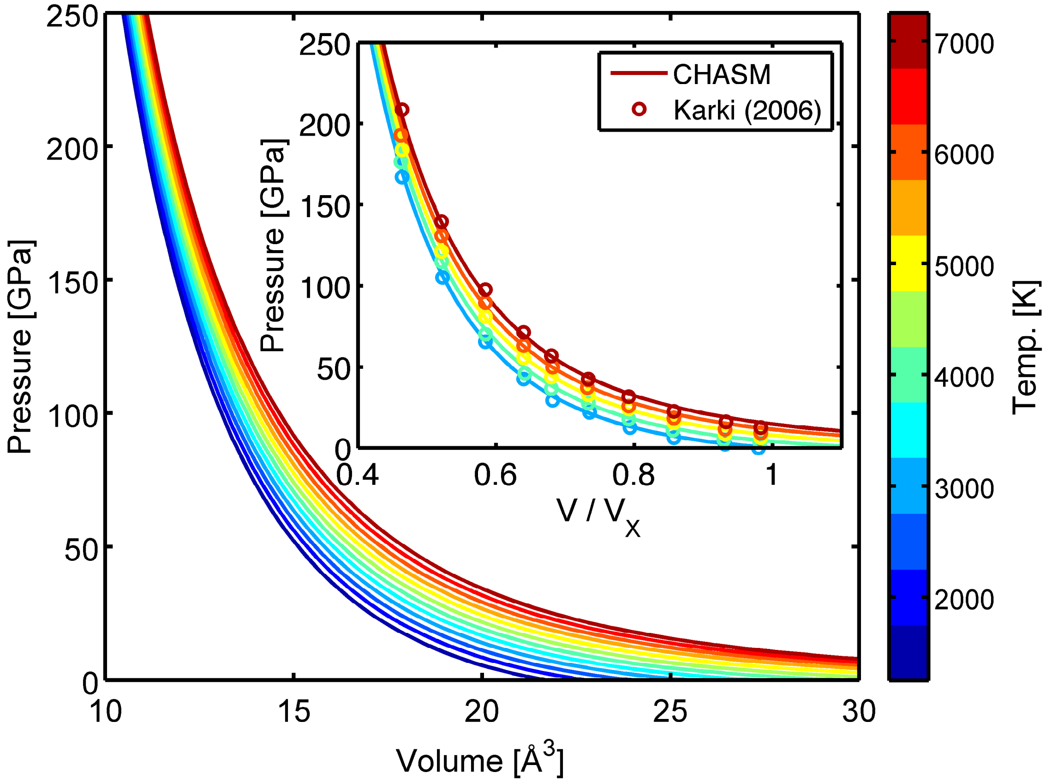

Figure 4.13: Resulting equation of state curves for MgO liquid over a range of temperatures. The curves are obtained by fitting third-order Birch-Murnaghan equations to the free energy curves determined by CHASM, from which the pressure curves are readily determined. The inset figure shows the same curves replotted against a relative volume, where the volume scale is given by the 3000K zero-pressure volume. Also plotted are the first-principles results from *Karki et al.* (2006), which our calculation is in strong agreement with, except for the value of our volume scale, which is 25.4 $\mathring{A}^3$ as opposed to 27.4 $\mathring{A}^3$ from *Karki et al.* (2006).

way the evolution of coordination populations is a direct prediction of the model, where the coordination states are chosen so as to minimize the free energy.

In addition to representing coordination states, the CHASM also account for internal energy variations that depend on the average structure of the liquid. This is incorporated through the use of coordinated cation pair potentials. The pair potentials actually represent nearly the only input to the model that is unique to the liquid being calculated—all remaining differences are derived from these all important potentials. We also demonstrate for the first-ever CHASM represented liquid, MgO melt, how the pair potentials can be obtained by training their values on the known energy-volume curves for a variety of solid structures, which discretely sample periodic examples from generally disordered structural continuum that is available to the liquid. By obtaining all of the input variables for the CHASM from solid structures, we have therefore generated a model that is fully predictive for liquid structure and thermodynamics, not requiring any input from liquid measurements (though it will be possible, but not necessary, to incorporate information from liquid experiments to adjust the pair potentials and improve the model).

Finally we demonstrate the use of the CHASM to calculate equations of state using MgO as an example. By design, the CHASM relies entirely on analytic function evaluations and simple 1D integrals, and thus computation remains rapid. The CHASM can obtain a converged calculation for a single state point (with a particular volume, temperature, and composition) in roughly one to a few minutes on a standard desktop processor. We show how the resulting prediction of coordination state evolution compares favorably with the orders of magnitude more time-consuming first-principles calculations. We also produce a set of predicted equation of state isotherms which match the first-principles results nearly perfectly after accounting for a shift in the zero-pressure volume scale.

In future work, we plan to apply this framework to the silica system, and then use it to explore thermodynamic properties along the $\mathrm{MgO–SiO_2}$ binary. Given that we have a method for describing the free energy surface of the liquid, we should also be able to look into the possibilities of making melting curve calculations, when combined with models for the solid free energies. Once multiple oxide components are introduced to the calculation, it may be important to improve the method of training pair potentials to allow for directly fitting the intermediate composition structures, rather than relying solely on the endmember description. Additional work should be put in to improving the internal degrees of freedom term in the free energy. There are also gains that can be made in implementation, potentially decreasing calculation times by a further factor of 3 to 10. Finally, we expect in the near future to begin the challenging process of incorporating FeO as a component, as it is much more complex than the other oxides, but crucial to our understanding of early Earth evolution. With its multiple internal spin state that can drastically effect local volumes, the Fe cations will have an added dimension to the available states, populating a range of oxygen coordination numbers while simultaneously populating a few discrete spin states.

— Appendices —

4.A Generalized Hard Sphere Mixture

The complete set of expressions for the equation of state of a hard sphere mixture is presented in *Mansoori et al.* (1971). For completeness, we include these expressions here, which represent the configurational free energy contribution ΔF_{HS} to the total free energy. We start with the expression for the packing fraction:

$$\eta_i \equiv \frac{V_{\text{HS},i}}{V} = x_i \frac{4\pi}{3V} R^3_{\text{HS},i} \quad \text{where} \quad \eta = \sum_i \eta_i \tag{4.17}$$

The compressibility Z is expressed as a function of the packing fraction:

$$Z = \frac{PV}{kT} \approx [1 + \eta + \eta^2 - 3\eta(y_1 + y_2\eta) - \eta^3 y_3](1-\eta)^{-3} \tag{4.18}$$

where the needed additional relations are:

$$\begin{aligned} y_1 &= \sum_{i=1} \sum_{j>i} \Delta_{ij} (R_i + R_j)(R_i R_j)^{-1/2} \\ y_2 &= \sum_{i=1} \sum_{j>i} \Delta_{ij} \sum_{k=1}^{N} \left(\frac{\eta_k}{\eta}\right) \frac{(R_i R_j)^{1/2}}{R_k} \\ y_3 &= \left[\sum_{i=1} \left(\frac{\eta_i}{\eta}\right)^{2/3} x_i^{1/3} \right]^3 \\ \Delta_{ij} &= \left[\frac{(\eta_i \eta_j)^{\frac{1}{2}}}{\eta}\right] \left[\frac{(R_i - R_j)^2}{R_i R_j}\right] (x_i x_j)^{\frac{1}{2}} \end{aligned} \tag{4.19}$$

These are all combined to express the contribution to the free energy and entropy of the liquid:

$$\begin{aligned}\frac{\Delta F_{HS}}{kT} = \frac{F_{id}}{kT} - \frac{3}{2}(1 - y_1 + y_2 + y_3) + (3y_2 + 2y_3)(1-\eta)^{-1} + \\ \frac{3}{2}(1 - y_1 - y_2 - \frac{1}{3}y_3)(1-\eta)^{-2} + (y_3 - 1)\log(1-\eta)\end{aligned} \tag{4.20}$$

$$\Delta S_{HS} = k \log Z - \frac{(F_{HS} - F_{id})}{T} \tag{4.21}$$

4.B Hard Spheres with Structural Perturbation

The variational approach to hard spheres allows the incorporation of a structural perturbation into the free energy expression, which captures the dependence of the internal energy on the structure of the liquid. This perturbation method was developed by *Mansoori and Canfield* (1969), and the resulting expressions are shown here.

We begin by approximating the structural energy contribution using the radial distribution function $g(r)$, together with pair potentials $u(r)$:

$$\begin{aligned}F \approx F_{HS} + F_{\text{struc}} = F_{HS} + \int_0^\infty P(r)u(r)dr \\ \approx F_{HS} + 4\pi\rho \int_{R_{min}}^\infty r^2 u(r) g(r) dr\end{aligned} \tag{4.22}$$

Mansoori and Canfield (1969) showed that the above integral for the structural perturbation energy E_{struc} can be transformed using a Laplace transformation, yielding:

$$F \approx F_{HS} + 4\pi\rho R_{HS}^3 \int_0^\infty U(s)G(s)ds \tag{4.23}$$

It turns out that while expressing the radial distribution function directly is quite challenging, relatively simple analytic approximations exist for its Laplace transform (which is an exponential integral transform similar to a Fourier transform, but one where the exponential weighting function is real valued and thus imposes a decaying rather than oscillatory envelope). We can understand this on an intuitive level, since the radial distribution function is a function that inherently decays to an asymptotic constant value of one. Therefore, by expressing the RDF in terms of its Laplace transform, it is ensured that the RDF will necessarily possess the required asymptotic behavior for large separation distances.

$G(s)$ is the Laplace transform of the hard sphere radial distribution function and $U(s)$ is the inverse Laplace transform of the pairwise potential energy function, defined by:

$$G(s) = \int_1^\infty \exp(-sx) g_0(x) x dx \tag{4.24}$$

$$xu(x) = \int_0^\infty \exp(-sx) U(s) ds \tag{4.25}$$

These expression for $G(s)$ has a simple functional form given by Percus-Yevick theory, and can be found in any standard text on the hard sphere model. (One easily readable account is given by *Yuste et al.* (1998). The inverse Laplace transform is a standard integral, and thus we can obtain the expression for an exponential, appropriate for the generalized Morse potential, using simple integral tables or Mathematica.

4.C Representing Variable Coordination

In order to carry out the structure perturbation calculation, we must have an expression for the pair potential between every possible pair of particles. This is not generally practical because the solid structures generally sample only a single coordination state, and thus do not constrain the energetic cost of two different coordination states interacting. To handle this challenge, the empirical molecular dynamics community long ago developed the practice of obtaining rules for "mixing" the pair potentials of two different particles to estimate an effective cross-pair-potential. The most accurate of the available mixing rules are given by *Kong* (1973), and we summarize the results of the mixing rules below, considering interactions between particles of type 1 and 2:

$$\begin{array}{rl} \text{attractive mixing:} & \dfrac{1}{\sigma_A^{12}} = \dfrac{1}{\sigma_A^{11}} + \dfrac{1}{\sigma_A^{22}} \quad , \quad \epsilon_A^{12} = \sqrt{\epsilon_A^{11}\epsilon_A^{22}} \\ \text{repulsive mixing:} & \sigma_R^{12} = \dfrac{1}{2}\left(\sigma_R^{11} + \sigma_R^{22}\right) \quad , \quad \left(\dfrac{\epsilon_R^{12}}{\sigma_R^{12}}\right)^{\sigma_R^{12}} = \sqrt{\left(\dfrac{\epsilon_R^{11}}{\sigma_R^{11}}\right)^{\sigma_R^{11}} \left(\dfrac{\epsilon_R^{22}}{\sigma_R^{22}}\right)^{\sigma_R^{22}}} \\ \text{simple mixing terms:} & \sigma_A^{-1}, \;\; \log(\epsilon_A), \;\; \sigma_R, \;\; \sigma_R \log(\epsilon_R/\sigma_R) \end{array} \tag{4.26}$$

the simple mixing terms therefore represent the quantities that can be mixed through simple arithmetic means.

4.D Free Energy Contribution of Bond-Angle Deviations

The free energy contribution due to the freedom of bond-angle is approximately determined using elementary quantum mechanics. We think of the oxygens as being constrained to lie on the surface of a sphere whose radius is the bond length. The oxygens are not allowed to freely wander along the full surface of the sphere, but are rather confined to a portion of it defined by the average locations of the neighboring bonded oxygens. Thus we can imagine each oxygen as being confined to portion of the bonding sphere whose area is just the total area divided by the coordination number:

$$A_{\text{oxy}} = \frac{4\pi l^2}{N_{cn}} = 2\pi l^2(1 - \cos\phi_{\text{oxy}}) \tag{4.27}$$

Neglecting the detailed shape of the confinement area, we can approximate this area on the sphere as a spherical cap, whose opening angle is ϕ_{oxy}, given above.

When considering the true confinement area, we must recognize that the neighboring bonded oxygens will avoid overlapping one another which effectively reduces the size of the confinement area. The expression for this is given by:

$$\phi_{\text{oxy}} = \cos^{-1}(1 - 2/N_{cn}) \quad \text{and} \quad \Delta\phi_{\text{NN}} = \sin^{-1}(r_{\text{oxy}}/l) \tag{4.28}$$

Thus the adjusted confinement area for each bonded oxygen is just:

$$A_{\text{conf}} = 2\pi l^2(1 - \cos\phi_{\text{conf}}) \quad \text{and} \quad \phi_{\text{conf}} = \phi_{\text{oxy}} - \Delta\phi_{\text{NN}} \tag{4.29}$$

Now that we have an estimate of the confinement region, we can calculate the free energy contribution by approximating this as a particle in a two-dimensional box. Neglecting the effect of the curved surface, the 2D single particle in a box expression is:

$$F^{1}_{\text{bond Ang}} = -kT \log\left(\frac{mkTA_{\text{conf}}}{2\pi\hbar^{2}}\right) \tag{4.30}$$

where the value for the confinement area is given above. The total free energy is given by the sum over each particle (coordinated oxygen), but we must also account for the fact that the oxygens are shared between neighboring cations. Therefore, to avoid over-counting, we also multiply by the factor $f = n_{\text{oxy}}/N_{cn}$, yielding the final expression for the bond-angle freedom:

$$F_{\text{bond Ang}} = fN_{cn}F^{1}_{\text{bond Ang}} = n_{\text{oxy}}F^{1}_{\text{bond Ang}} \tag{4.31}$$